Available online at www.sciencedirect.com
SCIENCE DIRECT®
ELSEVIER
Nuclear Instruments and Methods in Physics Research A 519 (2004) 558–609
NUCLEAR INSTRUMENTS & METHODS IN PHYSICS RESEARCH Section A
www.elsevier.com/locate/nima

Experiment E835 at Fermilab

G. Garzoglio[a], K. Gollwitzer[a], A. Hahn[a], M. Hu[a], P. Marsh[a], J. Peoples[a], S. Pordes[a], J. Streets[a], S. Werkema[a], M. Ambrogiani[b], M. Andreotti[b], W. Baldini[b], D. Bonsi[b], M. Bombonati[b], D. Bettoni[b], R. Calabrese[b], G. Cibinetto[b], P. Dalpiaz[b], E. Luppi[b], M. Martini[b], M. Negrini[b], M. Savrié[b], G. Stancari[b], L. Tomassetti[b], A. Buzzo[c], M. Lo Vetere[c], M. Macrí[c], M. Marinelli[c], M. Pallavicini[c,*], C. Patrignani[c], E. Robutti[c], A. Santroni[c], G. Lasio[d], M. Mandelkern[d], W. Roethel[d], J. Schultz[d], M. Stancari[d], G. Zioulas[d], M. Graham[e], R. Rusack[e], S.H. Seo[e], T. Vidnovic III[e], X. Fan[f], S. Jin[f], D. Joffe[f], J. Kasper[f], P. Maas[f], Z. Metreveli[f], T. Pedlar[f], J. Rosen[f], P. Rumerio[f], K.K. Seth[f], A. Tomaradze[f], I. Uman[f], P. Zweber[f], S. Argirò[g], S. Bagnasco[g], G. Borreani[g], R. Cester[g], F. Marchetto[g], E. Menichetti[g], R. Mussa[g], M.M. Obertino[g], N. Pastrone[g]

[a] *Fermilab, USA*
[b] *I.N.F.N. and University of Ferrara, Italy*
[c] *I.N.F.N. and University of Genova, Via Dodecaneso 33, Genova 16146, Italy*
[d] *University of California at Irvine, USA*
[e] *University of Minnesota, USA*
[f] *Northwestern University, USA*
[g] *I.N.F.N. and University of Torino, Italy*

Received 9 October 2003; accepted 9 October 2003

Abstract

We provide a comprehensive description of experiment E835 at Fermilab, a high-precision experimental study of charmonium bound states. The $\bar{c}c$ states are formed in $\bar{p}p$ annihilations of cooled antiprotons stored in the Fermilab Antiproton Accumulator using a dense internal hydrogen gas-jet target. We describe the experimental strategies adopted for detecting the tiny $\bar{c}c$ resonant signals in the huge non-resonant hadronic background, and for measuring resonance parameters with high precision.

1. Introduction

Experiment E835 [1] at Fermilab, a major upgrade of its predecessor E760 [2], is devoted to the high precision study of the charmonium spectrum. In this experiment $\bar{c}c$ states are formed

*Corresponding author.
E-mail address: marco.pallavicini@ge.infn.it (M. Pallavicini).

0168-9002/$ - see front matter © 2003 Elsevier B.V. All rights reserved.
doi:10.1016/j.nima.2003.10.089

in $\bar{p}p$ annihilations when the cooled $\bar{p}$ beam coasting in the Fermilab Antiproton Accumulator (AA) intersects a dense H_2 molecular cluster gas-jet target; $\bar{c}c$ states are detected in the large non-resonant hadronic background by observing their decay into electromagnetic final states using a non-magnetic spectrometer. We took data during runs in 1996–97 and 2000 in which integrated luminosities of 141.4 and 113.2 pb^{-1} were collected respectively.

We discuss the specific features of the experimental technique, the detector and its performance, and the data reconstruction and analysis methods, including details that are usually omitted in papers reporting physics results. For a critical review of charmonium spectroscopy using $\bar{p}p$ see Ref. [3].

The paper is structured as follows:

In Section 2 we describe the method used to measure resonance parameters, and discuss the sources of experimental systematic error in these measurements.

Section 3 describes the operation of the Antiproton Accumulator (AA) for experiment E835, in particular the effects of beam manipulations on the quality of the measurements. We discuss the measurement of the beam energy and the beam-energy spread, which determine our ability to measure masses and widths of resonances.

In Section 4 we describe the gas-jet target and its effects on the antiproton beam lifetime and beam-gas background.

The detector is described in Section 5; we discuss performance, calibration procedures, and performance stability and aging in the high-luminosity environment of E835.

Section 6 is devoted to the trigger, which operates with high rejection and high efficiency in an extremely-high rate and completely-asynchronous environment. We discuss its efficiency and stability during the long period of data taking.

Section 7 describes the data acquisition system (DAQ), including hardware and software components.

Section 8 describes offline computation and data handling, including detector calibration and alignment, charged particle tracking, γ–π^0 separation and electron identification.

The last section discusses simulations and their accuracy in reproducing real data.

2. Experimental technique

Charmonium states are formed in $\bar{p}p$ collisions at the intersection of the $\bar{p}$ beam circulating in the AA with an internal hydrogen gas-jet target.

We have the Breit–Wigner formula:

$$\sigma_{BW}\left(\sqrt{s}\right) = \frac{\pi(2J+1)}{s-4m_p^2}\frac{\Gamma_R^2 B_{in} B_{out}}{\left[\sqrt{s}-M_R\right]^2+\Gamma_R^2/4} \quad (1)$$

where M_R and Γ_R are the mass and width of the resonance, B_{in} and B_{out} are the branching ratios to initial and final states, J is the resonance spin, m_p is the proton (and antiproton) mass, and $\sqrt{s}$ is the center-of-mass (cm) energy.

For all charmonium states, the cross-section is six to eight orders of magnitude smaller than the non-resonant $\bar{p}p$ cross-section. Therefore it is very difficult to observe resonances by studying hadronic final states.[1] However clear signals are achievable in electromagnetic final states, as first shown by R704 [4] at CERN, in both exclusive ($e^+e^-, \gamma\gamma, J/\psi\gamma, J/\psi\pi^0$) and inclusive ($J/\psi X, J/\psi \to e^+e^-$) reactions.

Each charmonium resonance is studied by sweeping the $\bar{p}p$ cm energy across the resonance region and measuring cross-sections of selected channels as a function of cm energy. Resonance parameters are extracted from the measured excitation curves using the Maximum Likelihood Method.

The antiproton beam has a momentum spread and the observed excitation curve is the convolution of Eq. (1) with the normalized (cm) energy distribution $G\left(\sqrt{s'}-\sqrt{s}\right)$, where $\sqrt{s}$ is the nominal cm energy.

$$\sigma\left(\sqrt{s}\right) = \varepsilon_{out}\alpha_{out}\int_0^\infty \sigma_{BW}\left(\sqrt{s'}\right) \times G\left(\sqrt{s'}-\sqrt{s}\right) d\sqrt{s'} \quad (2)$$

[1] Several hadronic channels such as $\bar{p}p \to \Phi\Phi \to 4K^{\pm}$ may demonstrate resonant features.

where ε_{out} and α_{out} are the detection efficiency and geometrical acceptance for the particular final state.[2]

At each center of mass energy point, $\sqrt{s_i}$, the expected number of events identified for a given final state is given by

$$N_i = \int_t \mathscr{L}_i(t) \times \left[\sigma\left(\sqrt{s_i}\right) + \sigma_{bck}\left(\sqrt{s_i}\right)\right] dt \quad (3)$$

where $\mathscr{L}_i(t)$ is the instantaneous luminosity, σ_{bck} is the effective background cross-section and $\sigma\left(\sqrt{s_i}\right)$ is given by formula (2). From the beam momentum distribution (see Section 3) and the background cross-section, which is measured with data taken well off resonance, the resonance parameters are extracted from measurements of N_i. The area under the excitation curve is given by:

$$A = \int_0^\infty \sigma\left(\sqrt{s}\right) d\sqrt{s} = \frac{\pi}{2}\sigma_{peak}\Gamma_R, \quad (4)$$

where

$$\sigma_{peak} = \frac{4\pi(2J+1)B_{in}B_{out}\alpha_{out}\varepsilon_{out}}{M_R^2 - 4m_p^2}. \quad (5)$$

Our method for measuring Γ_R depends on the relative values of Γ_R and Γ_B, the full-width at half-maximum (FWHM) of the cm energy distribution $G\left(\sqrt{s'} - \sqrt{s}\right)$. When the cm energy distribution is narrow compared to the excitation curve,[3] we measure Γ_R from the shape of the excitation curve given by Eqs. (1)–(3), which depends on $G\left(\sqrt{s'} - \sqrt{s}\right)$ but is independent of efficiency, acceptance and the absolute value of the cross-section.

For relatively small Γ_R we rely on Eqs. (4) and (5) as shown in [2], where we measure the J/ψ width ($\approx$100 keV) with $\Gamma_B \approx 500$ keV. The ratio σ_{peak}/A is independent of $G\left(\sqrt{s'} - \sqrt{s}\right)$ but the efficiency, acceptance, absolute value of the measured cross-sections and branching ratios must be known. Stable running conditions and high statistical accuracy are necessary.

Knowledge of efficiencies, acceptances and of the cm energy distribution $G\left(\sqrt{s'} - \sqrt{s}\right)$ are crucial for measurements of partial widths and branching ratios. Fig. 1 shows the distribution of beam widths for all data taken in 1996–97.

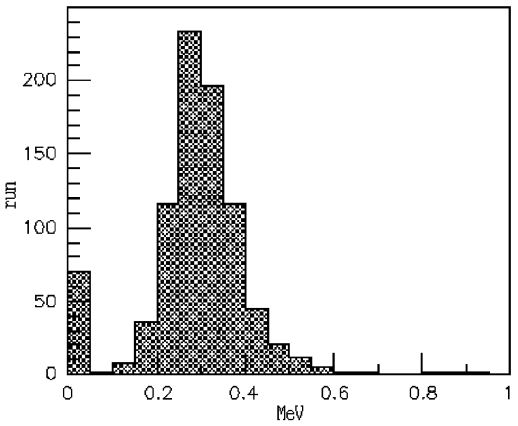

Fig. 1. Distribution of the center of mass energy spread (r.m.s.) for all data taken in 1996–97. The artifact at zero width is due to a small fraction of runs for which this information was not available.

3. The Fermilab antiproton beam

The Fermilab Antiproton Accumulator (AA) is a storage ring designed to accumulate and cool $\bar{p}$ at the fixed energy of 8.9 GeV. In order to provide beam in the charmonium energy range, it is operated in a non-standard way, which we briefly describe. For further details see Ref. [2] and references therein.

The AA is initially set at its design energy of 8.9 GeV to accumulate the desired number of antiprotons, typically $\approx 6 \times 10^{11}$. Stacking rates range from 2×10^{10} to 4×10^{10} $\bar{p}$ per hour.[4] The $\bar{p}$ are then decelerated to the desired energy with an RF cavity operating at the second harmonic of the beam revolution frequency f and with a maximum RF voltage of about 3 kV, allowing a deceleration rate of about 20 MeV/s. As the $\bar{p}$ are decelerated, the magnetic fields in the magnets are varied accordingly. The appropriate current ramps for

[2] Charmonium states are narrow enough so that the $\sqrt{s'}$ dependence of ε_{out} and α_{out} can be neglected.

[3] For negligible Γ_B it can be taken as $\delta\left(\sqrt{s'} - \sqrt{s}\right)$, hence $\sigma \propto (\sigma_{BW} + \sigma_{bck})$.

[4] 10^{10} $\bar{p}$ circulating in the AA correspond to about 1 mA current.

the dipole and quadrupole magnets are determined empirically during dedicated deceleration studies.

The AA stochastic cooling system is essential to the success of the experiment. The transverse cooling systems counteract the growth of the beam emittance due to the multiple scattering of the $\bar{p}$ with the target and with the residual gas in the machine, while the momentum cooling serves both to compensate for the energy loss in the target and to achieve the small rms energy spread shown in Fig. 1. The stochastic cooling system is able to achieve the small beam momentum spread when the RF is reduced to nearly 0 V. The beam effectively has no bunch structure and along with the gas jet provides constants interactions.[5]

The typical vacuum in the accumulator ring is 3×10^{-10} Torr giving a beam lifetime of ≈ 1000 h with the jet target off.

The experiment is located in a low dispersion region of the AA, where a $\Delta p/p$ of 10^{-4} produces a transverse displacement of less than 50 μm.

As we saw in Section 2, the average beam energy and the beam energy spread are crucial for the determination of the mass and width of a resonance. In particular, the precision of the average beam-energy measurement determines that of the mass measurement, while the precision of the beam-width determination strongly affects that of the width measurement for narrow resonances. The next two sections describe how these two quantities are measured. See [2] for further details.

3.1. Measurement of the average beam energy

The antiproton energy is determined from its velocity $c\beta = fL$, where L is the orbit length. L is written as $L = L_0 + \Delta L$ where L_0 is the reference orbit length and ΔL the displacement. To measure β, f and L are determined. The revolution frequency f is determined from the longitudinal Schottky noise [5] spectrum, obtained using a spectrum analyzer and a dedicated beam pick-up; Fig. 2 is a spectrum for the 127th harmonic of f.

[5] A small RF signal is needed for the beam position monitoring system.

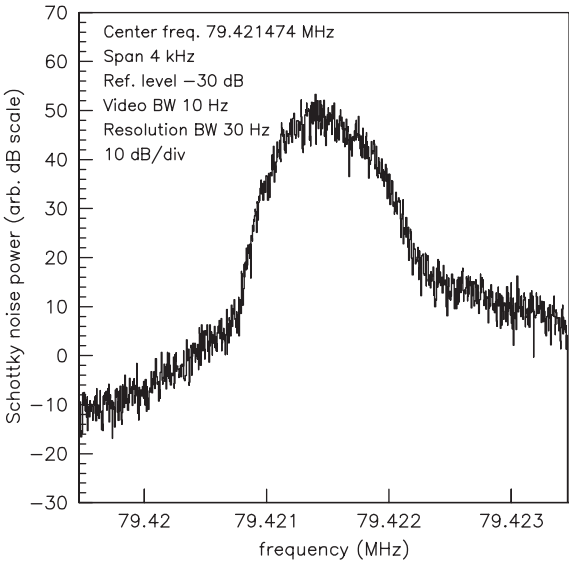

Fig. 2. Spectrum analyzer measurement of the longitudinal Schottky noise power spectrum of the antiprotons for a beam momentum of 6232 MeV/c. The spectrum analyzer was tuned to the 127th harmonic of the beam revolution frequency.

The reference orbit length L_0 is calculated from an energy scan at the ψ' using the known mass of the ψ' resonance. Neglecting the contribution of the error on f ($\delta f_0/f_0 \approx 1.5 \times 10^{-7}$), the uncertainty in L_0 is

$$\frac{\delta L_0}{L_0} = \frac{M_{\psi'}}{\gamma_{\psi'}^3 \beta_{\psi'}^2 m_p^2} \delta M_{\psi'}. \quad (6)$$

The error of 0.1 MeV/c^2 for the ψ' mass quoted in [6] yields an uncertainty of 0.67 mm for L_0 at $\sqrt{s} = M_{\psi'}$.

To measure the beam energy we determine f and ΔL, which can be as much as 2 mm. To determine the beam orbit, the AA is equipped with 48 beam position monitors (BPM).[6] The overall orbit-length uncertainty is ± 1 mm, corresponding to an uncertainty of ± 0.05 MeV at the J/ψ energy and ± 0.15 MeV at the ψ' energy; this is the largest

[6] Ideally, the BPMs should be positioned in the centers of the bending magnets. This is not possible and they are placed on either side of the magnets; the BPM data are used to determine the beam orbit in a piecewise manner or indirectly in a constrained fit using a detailed model of the AA lattice.

systematic uncertainty in the charmonium mass measurements.

3.2. Measurement of the beam energy spectrum

The beam energy spectrum is also determined from the beam longitudinal Schottky noise spectrum, e.g. Fig. 2. In particular, the quantity dp/p is related to df/f by the equation:

$$\frac{dp}{p} = -\frac{1}{\eta}\frac{df}{f} \tag{7}$$

where the slip factor η is given by

$$\eta = \frac{1}{\gamma_t^2} - \frac{1}{\gamma^2} \tag{8}$$

and γ_t, the *gamma factor* at the transition energy, is a parameter determined by the machine lattice [7]. Since df/f is well measured, to obtain the beam energy spectrum we must determine η as a function of the beam energy. We measure η with two different techniques:[7] (1) measurement of the synchrotron frequency; (2) direct measurement of γ_t.

3.3. Determination of η from the synchrotron frequency as a function of peak RF voltage

When the radio frequency (RF) is on, the energy of an orbiting particle oscillates about the synchronous energy with a characteristic synchrotron frequency f_s, determined by:

$$f_s^2 = -\frac{eV_{RF}}{E}\frac{f_{RF}^2}{2\pi h}\frac{\eta\cos(\phi_s)}{\beta^2} \tag{9}$$

where V_{RF} and f_{RF} are the peak RF voltage and RF frequency, E is the beam energy, $h = 2$ is the harmonic number, ϕ_s is the synchronous phase, which for stationary beams is 0 above transition ($\gamma > \gamma_t$) and π below transition.

The synchrotron frequency is determined with a precision of 1%. The uncertainty in η is dominated by the uncertainty in the RF voltage (5%). The fit to η is shown in Fig. 3.

[7] A third method, the *double scan*, was developed by E760 for the measurement of the J/ψ and ψ′ widths. See Ref. [2] for details.

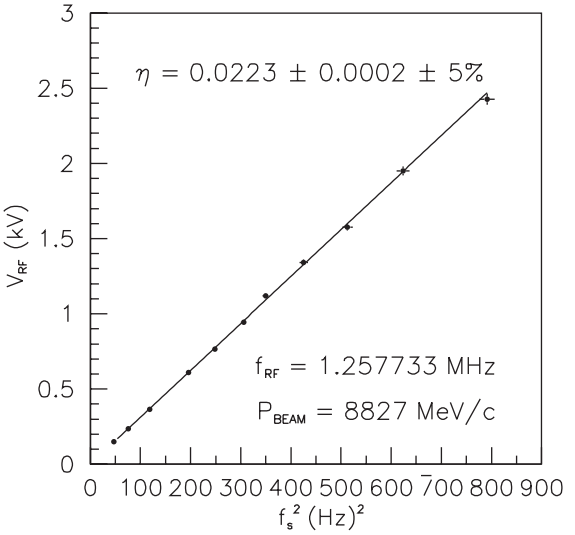

Fig. 3. Measurement of η at the injection energy from the synchrotron frequency. f_s^2 is plotted as a function of the peak RF voltage V_{RF}. A straight line fit yields the result shown.

3.4. Determination of η from γ_t

Eq. (8) shows that η can be determined from γ_t, which can itself be measured by slowly varying all of the dipole magnetic fields B together with the RF off and observing the resulting change in f, the relation being:

$$\frac{dB}{B} = \gamma_t^2\frac{df}{f}. \tag{10}$$

This method is unfortunately weaker than the previous because of large systematic errors in B. The uncertainties in η and γ_t are related by:

$$\delta\eta = \frac{2}{\gamma_t^3}\delta\gamma_t. \tag{11}$$

This method is used only to cross check the results from methods (1). An example of this method at the injection energy is shown in Fig. 4.

4. The jet target

In order to observe narrow $\bar{c}c$ states, a pure hydrogen target is required. Using heavier target nuclei would make the observation of narrow states difficult because of resonance broadening

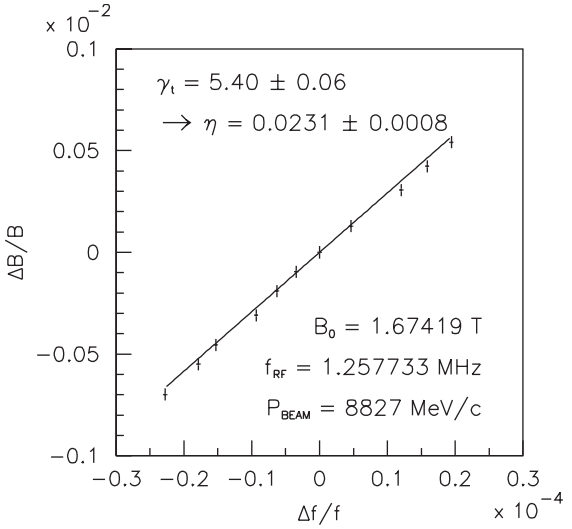

Fig. 4. Direct measurement of γ_t by changing the dipole B field and looking at the change in frequency f of the beam. The straight line fit yields a result compatible with that computed from the synchrotron frequency measurements.

due to the Fermi motion of the nucleons in the nucleus. Higher-Z nuclei would also reduce the $\bar{p}$ beam lifetime. With hydrogen, even the narrowest resonances can be directly scanned, since the measured width depends only on the beam characteristics, as shown in Section 2.

An internal hydrogen jet crossing the $\bar{p}$ beam at 90° was chosen. It allows continuous operation of the AA while providing luminosity adequate for studying the cross sections of interest (tens of nb to several pb). The typical instantaneous luminosity during data taking is 2×10^{31} cm^{-2} s^{-1}, corresponding to a minimum bias trigger rate of about 3 MHz.

The gas jet used for the E760 [8] and E835 [9] target is of the *cluster jet* type, in which the core of the jet is made up of microdroplets, or clusters, of condensed matter (in our case hydrogen). A cluster jet is produced by the isentropic expansion of a gas through a convergent-divergent nozzle in conditions of high pressure and low temperature (see Fig. 5). The sudden decrease in pressure and temperature caused by the expansion leaves the gas in a supersaturated state and favors the formation and growth of clusters whose size varies from 10^7 to 10^8 molecules [10,11].

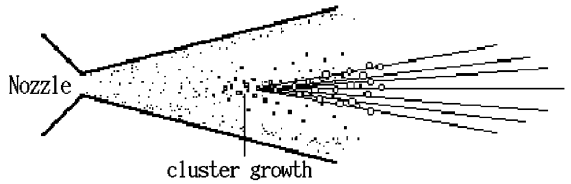

Fig. 5. Schematic view of the jet target nozzle. Its trumpet-like shape causes supersaturation of the gas, leading to formation of metastable microdroplets, which are much denser than the gas.

The clusters constitute the core of the gas flow exiting the nozzle. They have the remarkable property of a very narrow velocity distribution and form a high-density cone with directional spread of several degrees with respect to the axis. A set of collimators defines the jet that crosses the antiproton beam to less than 2° with respect to the axis. The portion of the jet at large angles is pumped away before it can enter the AA vacuum pipe.

The nozzle is trumpet-shaped with an opening angle of 3.5°, a divergent length of 8 mm and a throat diameter of 37 μm. The operating points for the nozzle pressure and temperature are based on the following considerations.

Because of the shape of the isentropes on the P–T diagram of hydrogen, the density of the jet is maximized when the expansion begins at the highest possible pressure and as close to the H_2 saturation curve as possible, i.e. at the lowest temperature for that pressure. A major upgrade was made to the target for E835 by incorporating a helium cryo-cooler as part of the final stage of the hydrogen line. This allows operation with hydrogen gas at temperatures down to 20° K, compared with E760, where the minimum temperature was set by the liquid nitrogen cooling system at ~89° K. We also acquired the capability of changing the P–T point where the expansion starts; as we reduce the pressure and temperature at the nozzle, following the saturation curve, we achieve correspondingly lower jet densities. In Fig. 6 we show the phase diagram for H_2, the operating points we utilized (open circles) and the jet density (upper curve) corresponding to each operating point.

To use the jet as a target inside the storage ring, we separate the cluster jet stream from the other

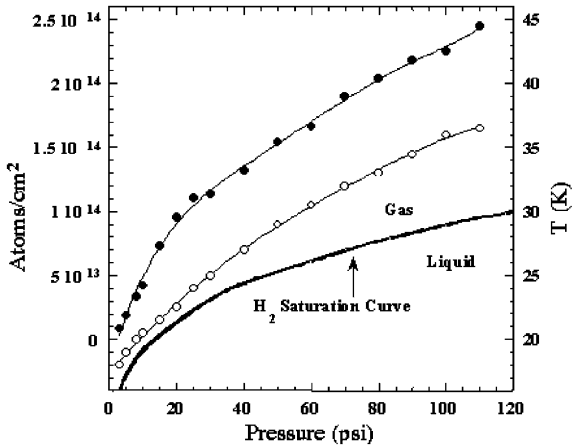

Fig. 6. The P–T phase diagram for H_2, the operating points we utilized (open circles) and the jet density (upper curve) corresponding to those operating points.

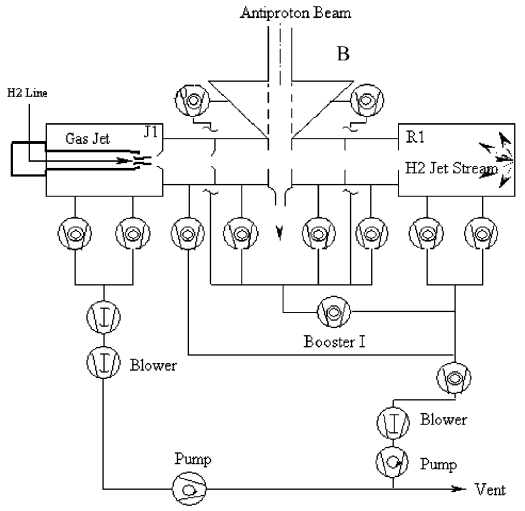

Fig. 7. Schematic layout of the jet target.

gas exiting the nozzle. This gas diffuses into the AA reducing the beam-lifetime and producing background interactions. We minimize the quantity of background gas by using a differential pumping system (see Fig. 7), in which the jet crosses a series of chambers which are independently evacuated. Ten turbo-molecular pumps (TMP) are installed directly onto the chambers. Eight of these have a capacity of 1000 l/s and two are rated for 3500 l/s. Because of the low compression ratio of TMPs for hydrogen, the system is designed to avoid limiting the pressure in the high vacuum zone of each pump due to the rough vacuum. This is achieved by using two additional TMPs, three positive-displacement blowers and two roughing pumps arranged in a cascade configuration. From the pressure inside the AA we infer that the quantity of hydrogen gas elsewhere in the machine is about 5% of that which constitutes the target. In other words, 95% of the interactions occur in the desired interaction region. This is a great improvement compared to E760 where the percentage of escaped gas was 40%.

Automatic control systems are used to set the pressure of the hydrogen line and the temperature of the nozzle within 0.5 psi and 0.05 K, respectively, with a response time of 10 s. (Other parameters which have an effect on the interaction rate, such as the beam current, vary with a time scale of hours). By adjusting the nozzle pressure and temperature as discussed above, we achieve densities from 1×10^{13} to 3.2×10^{14} atoms/cm^3. The latter is more than 5 times larger than the maximum density reached in E760 (6×10^{13} atoms/cm^3). The diameter of the jet in the interaction region (6 mm) is unchanged, as it is defined only by the geometry of the skimmer between the second and third vacuum chamber. By adjusting the density within these bounds, we maintain the instantaneous luminosity of the experiment at a constant value, typically 2×10^{31} cm^{-2} s^{-1}, even as the antiproton beam intensity diminishes because of interactions. Fig. 8 is an example from the run. The ability to vary the target density allows us to operate at maximum luminosity throughout a stack and effectively doubles the integrated luminosity we collect.

The gas jet beam-pipe wall is 0.18 mm LN316 stainless steel in the region where secondary particles pass into the main detector.

5. The detector

The detector is optimized to detect electromagnetic final states with two charged or neutral

particles forming a large invariant mass. It is designed to provide a large acceptance and to operate at high interaction rates. The capability for operation at high rates is achieved by segmenting the detectors and by equipping all channels with time-to-digital convertors (TDC) to allow rejection of out-of-time signals.

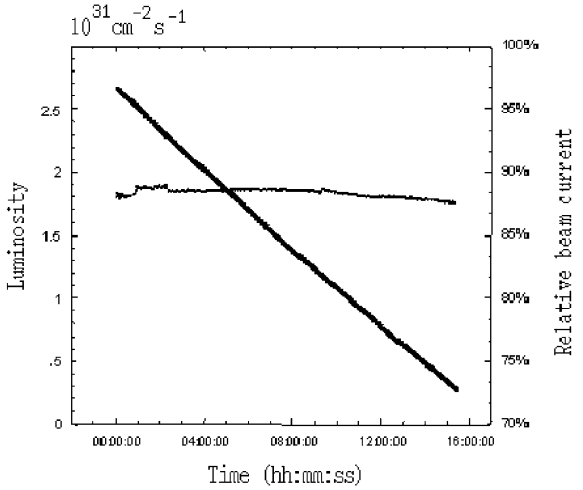

Fig. 8. The luminosity control system. As the beam current diminishes (linearly decreasing curve in units of number of circulating antiprotons), the instantaneous luminosity is kept constant by gradually increasing the jet density (the almost constant value shown by the flat curve corresponds to 1.9×10^{31} cm^{-2} s^{-1}).

The space available constrains the apparatus to be compact and led to the cylindrical, non-magnetic detector shown schematically in Fig. 9.

The innermost section of the detector is devoted to the charged particle trigger and tracking. During the 1997 run it was composed of three plastic scintillator hodoscopes, four layers of drift tubes (straws), a silicon-pad detector, a forward veto scintillation counter and a scintillating-fiber detector. For the year 2000 run the silicon detector was replaced by a second scintillating fibers detector. The inner detectors are fully contained in a cylinder of radius 17 cm and length 60 cm; their total thickness is less than 7% of a radiation length (X_0) for particles crossing at normal incidence.

A threshold Cherenkov counter provides triggering on electrons produced in J/ψ decays.

Electron and photon energies and directions are measured by two electromagnetic calorimeters that together give full acceptance between 2° and 70° in the laboratory frame.

The total integrated luminosity is measured by means of a luminosity monitor that is installed beneath the jet target body.

In the following sections each detector and its performance is described. Additional details are contained in the quoted references.

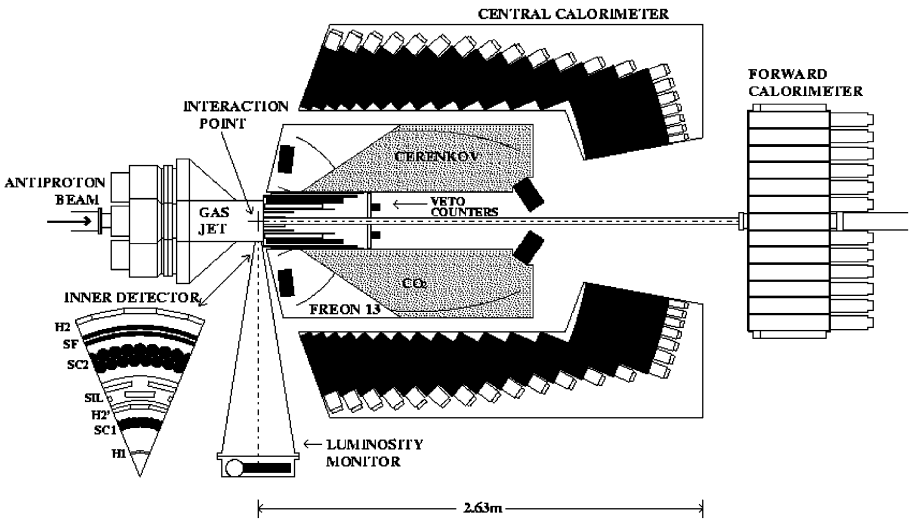

Fig. 9. Schematic side view of the E835 detector as it was during 1996/1997 run.

5.1. The scintillation hodoscopes and the veto counter

In the inner detector, we have three scintillator hodoscopes, H1, H2 and H2′. H1 is the innermost and consists of 8 plastic scintillators that together form a cone-shaped structure surrounding the segment of beam pipe attached to the jet target body. Its thickness is 2 mm and it provides full geometrical acceptance in ϕ and in θ from 9° to 65°.[8] The light yield from H1 is about 10–20 photoelectrons (p.e.) for a single minimum ionizing particle (m.i.p).

H2 is a cylindrical hodoscope (radius 17 cm) made of 32 elements whose dimensions are 4 mm × 3 cm × 60 cm, giving full geometrical acceptance in ϕ and between 12° and 65° in θ. The light yield is much better than H1 (50–100 p.e. per m.i.p) giving the best dE/dx measurement of the hodoscopes.

H2′ is similar to H2, with 24 elements 40.8 cm long on a 7 cm radius. It was added to improve the charged veto for purely neutral triggers (see Section 6.2 for details) and to improve the dE/dx measurement.

All three hodoscopes are used to trigger on charged particles (see Section 6.1), as a veto on neutral triggers (see Section 6.2) and to measure dE/dx. These measurements are an essential element of the electron identification algorithm (see Section 8.4).

An additional detector is installed as an end-cap of the inner tracking cylinder. It is made of 8 trapezoidal scintillators 2 mm thick, forming a complete annulus. This detector is used only as a charged particle veto in the very forward acceptance region (below 12°), where none of the tracking detectors are active.

5.2. The straw chambers

Two cylindrical chambers are built of proportional drift tubes (aluminized-mylar straws). They are used to determine the azimuthal angle ϕ of charged particles.

The mechanical design requirements are low mass, to minimize multiple scattering and photon conversions, and fine granularity, to limit occupancy of the elements. The thickness (at 90°) is 0.11% X_0 within the straws acceptance. Tight geometrical constraints determined a structure of two layers of 64 straw tubes in each chamber, staggered to resolve left-right ambiguity. The tubes are self-supporting between two grooved flanges that allow gas to flow continuously (see Fig. 10). Each flange (glass epoxy composite Stesalit 4411W, Switzerland) was made on a CNC machine in two pieces, which are glued together in a dedicated jig to guarantee precision in straw and pin positioning and alignment. Errors on the machined diameters and centers are measured to be typically ∼10 μm, never exceeding 50 μm.

Mylar tubes (80 μm thickness) with inner Al coatings (1000 atoms) [12] were inserted in the proper locations and glued onto the flange. On one of the two flanges, an evaporated layer of gold provides the grounding connection to all the tubes, made with a conductive glue (Tra-Duct 2902 TRACON, USA). 20 μm gold-plated tungsten wires (Luma Metall, Sweden) were strung with tensions of 20 and 40 g, in the inner and outer chamber respectively, and crimped into gold-plated copper pins (150 μm inner diameter) inserted in the dedicated holes of the flanges. In Fig. 10 a sketch of the mechanical structure is shown. The geometrical parameters of the two chambers are summarized in Table 1.

To withstand the high rates in the chambers (∼10 kHz/cm^2; ∼5 MHz@R∼3 cm and ∼1.5 MHz@R∼15 cm) and minimize pile-up, a custom analog bipolar integrated circuit, developed for high energy physics wire chambers at the University of Pennsylvania [13], was chosen. The chip used is the ASD-8B, an 8 channel amplifier-shaper-discriminator (Tektronix SHPi bipolar process), 1 cm × 1 cm (64 pin). Its fast peaking time (6–7 ns) and good double pulse resolution (25 ns) are crucial to avoid pile-up. The signal amplitude is about 20 mV/fC and the voltage programmable threshold is linear up to 30,000 e$^-$. The total power dissipation per channel is 23 mW.

[8] The polar angle θ is between the particle direction and the z axis defined by the $\bar{p}$ direction; we measure the azimuthal angle ϕ from the x axis defined by the hydrogen jet direction.

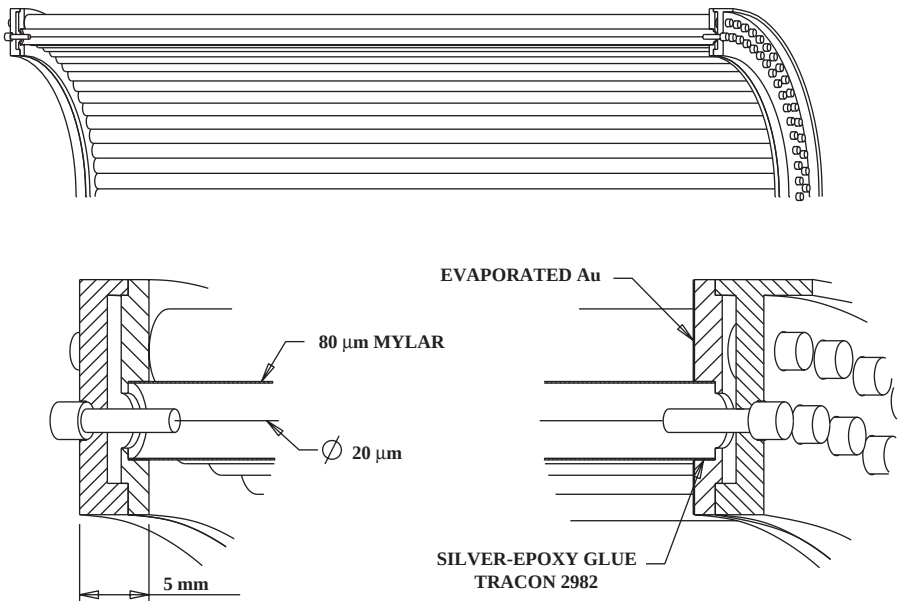

Fig. 10. Sketch of the mechanical structure of a Straw Chamber.

Table 1
Chamber radii, coverage in polar angle, straw diameters and lengths for the two straw chambers

	R (cm)	θ (°)	∅ (mm)	L (mm)
Inner	5.4	15–58°	5.0, 5.4	182
Outer	12.0	15–65°	11.1, 12.1	414

The front-end electronics are mounted on the downstream flange of each chamber to minimize oscillations and pickup. Due to the limited space available, only SMD components are used. Four different multilayer boards were designed:

- HV distribution boards, directly mounted on the pins (HV resistors and blocking capacitors): HV on the anode wires and the tubes grounded to the flange;
- test input circuits;
- ASD boards, where analog and digital ground are carefully separated;
- thresholds, low voltage regulators and output signals.

The last 3 boards are connected through SMD connectors (Conan-BERG Switzerland). These connectors are also used in the custom-made cables that run along the beam pipe to the receivers/stretchers located close to the apparatus. The output signals are differential small-diameter (2×2 mm by Polyfil-Switzerland) cables. Thresholds and test inputs are 50 Ω Fileca coaxial cables. The signals are processed in the counting room by 32-channel LRS multihit TDC 3377s used in common-stop mode.

The chambers were fully operational during testing of thresholds and noise after installation. When the apparatus was closed, a cable corresponding to $8+8$ tubes was badly connected, resulting in one dead/noisy octant in the inner chamber.

The chambers are operated with $Ar : C_4H_{10} : [(OCH_3)_2CH_2]$ 82:15:3, respectively at 1320 and 1530 V in the inner and outer chambers. This gas was chosen because it is efficient at relative low HV (drift velocity not saturated ~ 40 μm/ns) and effective in limiting radiation damage [14].

In the E835 acceptance region for $e^{\pm}$ ($15° < \theta < 60°$), without correction for dead channels and the inner chamber noisy octant (8% loss), the measured efficiency of reconstructing a track with at least two layers of straws is 97%, with an efficiency of about 89.8% per layer.

No channels failed during 1996/1997 run due to radiation damage (over 200 rads in nine months of data taking); we collected about 250 mC/cm during the run. Further details are given in Ref. [15].

5.3. The silicon detector

A silicon-pad detector designed to provide θ–ϕ association for charged tracks was installed for the 1997 run. Due to a problem in the cooling system at the very beginning of data taking, this detector was non-functional and we omit its description. Details about its design and performance in a test beam are found in Refs. [16,17].

5.4. The scintillating fibers

5.4.1. Detector design

The measurement of the θ of charged particles is performed using two cylindrical scintillating-fiber detectors. Each detector is made of two concentric layers of fibers wound around two coaxial cylindrical supports. The outer detector has 430 fibers per layer and covers the angular region between 15° and 65°; the inner one has 240 fibers per layer with an angular coverage from 15° to 55°. The layout is shown in Fig. 11. During the year 1997 data taking, only the outer detector was present; the inner detector was added for the year 2000 run. Scintillation light is detected by solid

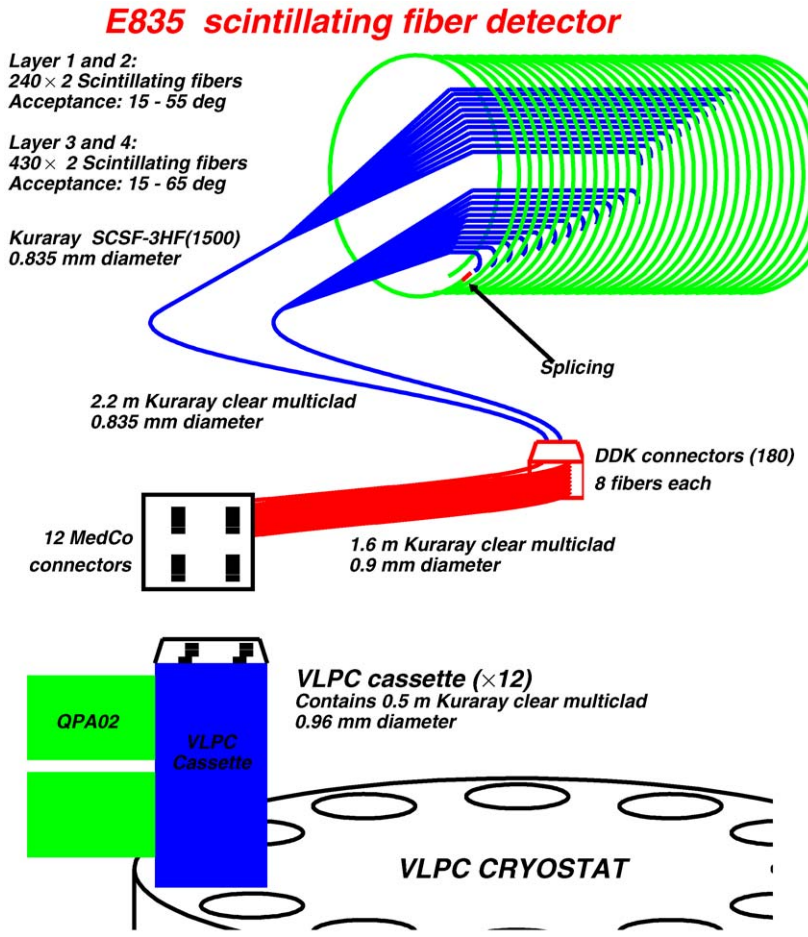

Fig. 11. Layout of the scintillating fiber detector.

state photosensitive devices, the Visible Light Photon Counters (VLPC) produced by Rockwell International. These photodetector have been chosen because of their very high quantum efficiency ($\approx 70\%$). Details of the fibers (Kuraray SCSF-3HF-1500), the cylindrical supports, the VLPCs (HISTE-V, EOC-low), the cryostat and the readout electronics are found in Refs. [18,19].

Each scintillating fiber (core diameter = 740 μm) is wound around one of the four support cylinders (radii 85.0 mm and 92.0 mm for the inner detector, 144.0 and 150.6 mm for the outer). The fibers are located in a set of U-shaped grooves, machined on the cylinders, of pitches 1.10, 1.19, 1.10 and 1.15 mm, respectively. The depth of the grooves varies linearly with the azimuthal coordinate ϕ, so that the fiber can overlap itself after one turn. The starting ϕ of each fiber is offset from the previous fiber so that the fibers do not overlap as they are bent from azimuthal to axial to emerge from the detector. On one end, the fibers are aluminized, to increase the light yield and reduce its dependence on position along the fiber; on the other end, they are thermally spliced to clear fibers. The clear fibers are 4 m long and bring the light to the VLPCs, which are housed in a cryostat at a temperature of 6.5 K.

The electronic signals generated by the VLPCs are amplified by QPA02 cards, designed at Fermilab [20]. After amplification, the signals are sent to custom-made discriminator-OR-splitter (discri-or) modules described in Section 6. This module provides an analog and a digital output for each input channel, together with the digital OR of all inputs. The analog signal is sent to an analog-to-digital converter (ADC), while the digital output was sent to a latch in the 1997 run and to a TDC in the 2000 run. For trigger purposes, the signals from the outer detector are grouped into 19 *bundles* of adjacent fibers. The digital OR of the signals from each bundle is sent to a TDC and to the first-level trigger logic of the experiment. The design parameters were determined from Monte Carlo calculations. Fig. 12a shows the number N of fibers of the outer detector (summed over both layers) whose core is intersected by a straight track originating from the interaction vertex as a function of θ. The dots represent the average over an arbitrary θ slice, while the error bars indicate the minimum and maximum possible values. The detector is designed so that the efficiency is better than 99% in average in the angular region between 15° and 50° and better than 90% in the large-θ region between 50° and 65°, as shown in Fig. 12b.

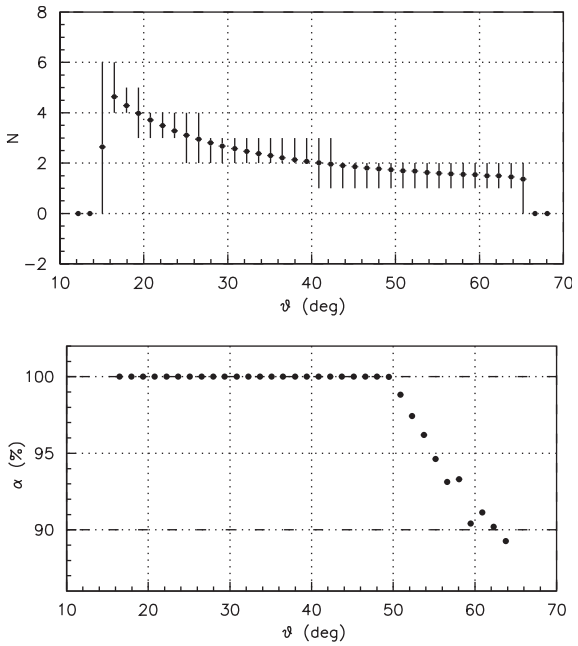

Fig. 12. (a) Number of hit fibers in the outer detector as a function of the polar angle θ; (b) Detector efficiency from Monte Carlo. Similar results are obtained for the inner detector.

5.4.2. Detector performance

5.4.2.1. Calibration. The signal generated by a track crossing one fiber, as seen at the input of the discriminator module, is typically 180 mV high and 80 ns wide, corresponding to a collected charge ≈ 0.2 nC.

In order to measure the one-p.e. equivalent in ADC counts (1 ADC count = 0.25 pC), we performed (for each channel) a LED test in the final readout configuration. The LED light produces a pulse-height spectrum in which one can identify the peaks due to 1, 2, and up to 4 p.e.

The pulse charge in ADC counts generated by a minimum-ionizing particle, is obtained by

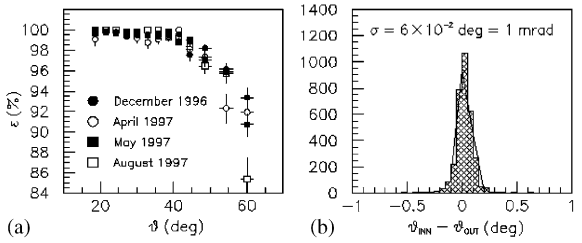

Fig. 13. Tracking performance of the scintillating fiber detector. On the left (a) the detection efficiency as a function of θ and time; on the right (b) the distribution of $\theta_{INN} - \theta_{OUT}$, the difference between polar angles measured by two layers of the outer detector.

studying a high-statistics hadronic sample of punch-through tracks in the electromagnetic calorimeter ($\approx 10^3$ events/fiber). More details are found in Refs. [18,19].

5.4.2.2. Efficiency and resolution. We measured the detection efficiency by using e^+e^- tracks from J/ψ and ψ' decays ($\approx 4 \times 10^4$ events) and $\bar{p}p$ elastic scattering events. For each track, we look for an associated hit in the scintillating-fiber detector above a given software threshold (typically, 0.2 m.i.p.), within a polar window of ± 50 mrad; the results are shown in Fig. 13a (1997 run) and in Fig. 14 (year 2000 run). The variations in efficiency were due to different run conditions (gate width of the ADCs) and the loss of channels resulting from power outages which caused warm-up of the VLPCs. The loss is particularly noticeable at large angles where there is less redundancy since the tracks intercept fewer fibers. The insertion of the inner detector increased the detection efficiency, as shown in Fig. 14. During the year 2000 run, the improved cryogenic system prevented major losses of channels; more than 95% of the channels were working at the end of the run.

The scintillating-fiber detector has by far the best spatial resolution in our apparatus. We can only measure the *intrinsic* tracking resolution, by comparing, for each detector, the measurements made by the two layers. In Fig. 13b we show, for the outer detector, the distribution of $\theta_{INN} - \theta_{OUT}$, where, for a given track, θ_{INN} (θ_{OUT}) is the polar angle measured by the inner (outer) layer of the

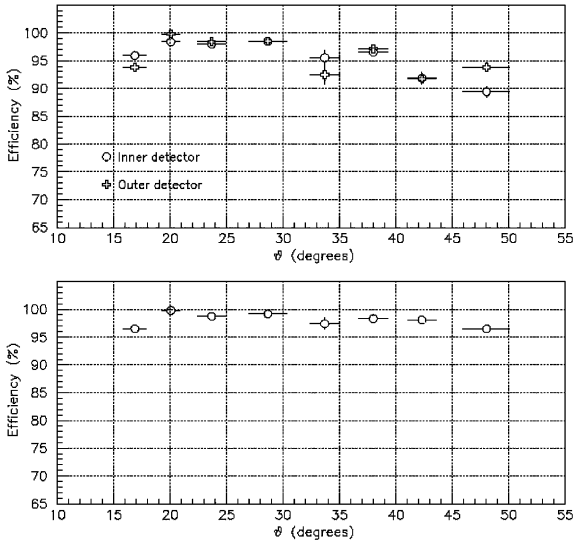

Fig. 14. Detection efficiency as a function of θ for the year 2000 run. On the top, the efficiencies of the two detectors; on the bottom, the global efficiency.

detector. The rms resolution, averaged over θ, is the standard deviation of this distribution divided by $\sqrt{2}$, which is (0.7 ± 0.1) mrad.

5.4.2.3. Pulse-height analysis. A background particularly important for E835 is e^+e^- pairs with small opening angle, generated by photon conversions or by Dalitz decays of neutral pions, which simulate single tracks. The scintillating-fiber detector provides two measurements, pulse height and granularity, that are helpful in identifying these pairs. When the opening angle of the e^+e^- pair is so small that just one cluster (defined as a set of adjacent hit fibers) is produced, the energy deposit is likely to be big; whereas when the pair separation is large, an extra cluster appears in the detector. This discrimination is shown in Fig. 15, where we plot $Q \sin\theta$ for single tracks (electrons or positrons) and for pairs, where a pair is defined as a charged track associated with a Cherenkov hit and pointing to a deposit in the central calorimeter kinematically consistent with a π^0. Q is the sum of the charges deposited in all the fibers in a $\pm 2^\circ$ window centered about the track. The $\sin\theta$ factor accounts for the path length variation in the fibers.

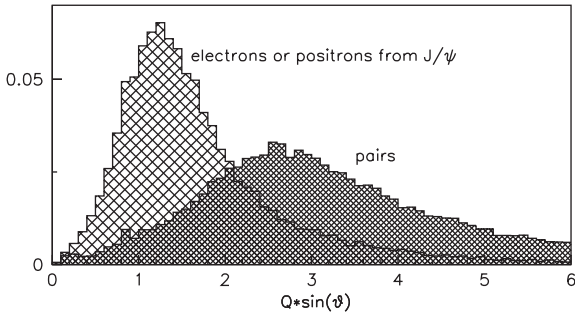

Fig. 15. Single/double-track discrimination from charge information in the scintillating-fiber detector. A sample of electrons and positrons is compared with a sample of pairs. The charge Q is multiplied by $\sin\theta$ to account for the θ dependence of the path length.

5.4.2.4. Timing resolution. To evaluate the intrinsic time resolution of the detector, we select those tracks that hit at least two fibers belonging to adjacent bundles, and are therefore read out by different TDC channels. The rms time resolution is the standard deviation, divided by $\sqrt{2}$, of the distribution in $t_i - t_{i+1}$, for tracks crossing both a fiber of bundle i and one of bundle $i+1$ ($i = 1, 18$). The intrinsic time resolution is approximately 3.5 ns and is mainly due to the decay time of the scintillator. More details about the performance of the detector during the year 2000 run can be found in Ref. [21].

5.5. The Cherenkov counter

A threshold gas Cherenkov counter is used in the charged particle trigger to select electrons from a large background of hadrons.[9] For general design considerations we refer to previous work [22,23] and only recall here the main characteristics of the counter.

The counter is operated at atmospheric pressure and room temperature, with different gases in the two cells, to optimize both the electron-detection efficiency and the π thresholds for best e/π separation.

[9] The E835 detector has no ability to distinguish e^+ from e^-, therefore everywhere in the text "electron" means either "electron" or "positron".

The counter occupies a cylindrical shell with inner radius of 17 cm and outer radius of 59 cm. It is subdivided into two separate gas-tight cells: the small θ cell filled with CO_2 at $15^\circ < \theta < 38^\circ$, and the large θ cell filled with Freon 13 (CF_3Cl) or Freon 12 (CF_2Cl_2) at $34^\circ < \theta < 65^\circ$. Each cell is optically segmented into eight sections, each section covering 45° in ϕ and equipped with one (small θ cell) or two (large θ cell) mirrors and one photomultiplier (PM). To minimize weight and amount of material traversed by the particles, the mechanical structure and the small θ mirrors are built of carbon fiber-epoxy composites. The surfaces are covered with a layer of plexiglas to improve their reflectance. The mirrors of the large θ cell are made of glass.

5.5.1. Optical system

In the source–detector configuration of E835, particles from $\bar{p}p$ collisions originate from an approximately point-like source ($5 \times 5 \times 6$ mm^3); thus the associated Cherenkov light can be focused by converging mirrors into a relatively small image at the PM window. To optimize light collection efficiency two schemes are used in the two cells.

In the large θ cell each of the 8 sectors in ϕ is equipped with a focusing spherical mirror and a plane mirror to reflect the light onto a PM placed in its own alcove of the counter's back wall (Fig. 16). The alcoves partly shadow the ϕ acceptance for $\theta > 60^\circ$ reducing it from 2π to about π.

The small θ cell contains 8 ellipsoidal mirrors, with common focus in the center of the interaction region, and their long axes tilted 8.5° relative to the beam line and equally spaced in ϕ (45°). With this geometry the second foci are at the vertices of a regular octagon, where the PM windows are placed. Light coming from an annular virtual source centered on the interaction region is directly focused onto the PM windows. The characteristics of the counter are summarized in Table 2.

5.5.2. UV coating

The mirrors are coated with a $\sim$1000 Å aluminum layer and protected against oxidation by anti-reflective thin films. This protective coating is MgF_2 on the ellipsoidal and on the plane mirrors, SiO_2 on the spherical mirrors. Fig. 17

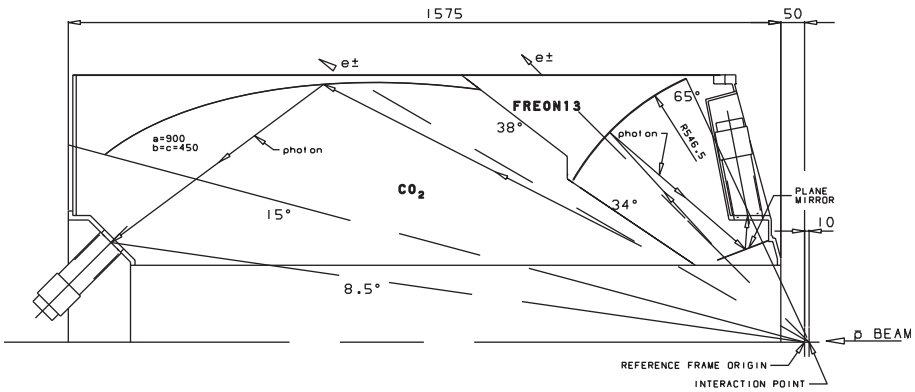

Fig. 16. Schematic side view of the Cherenkov counter.

Table 2
Geometrical and physical parameters for the Cherenkov counter

Angular aperture	$15^\circ < \theta < 38^\circ$	$34^\circ < \theta < 65^\circ$	
ϕ segmentation	$45^\circ \times 8$	$45^\circ \times 8$	
Gas (atm. press.)	CO_2	Freon 13	Freon 12
Refractive index	1.000410	1.000720	1.001080
θ_c	1.64°	2.17°	2.66°
π threshold (GeV/c)	4.873	3.677	3.003
Focusing mirrors	Ellipsoidal (plexi, carbon-fiber)	Spherical (glass)	
Thickness (mm)	4.3	3	
Parameters (mm)	Half-axes: $a = 900$, $b = c = 450$	Radius: $r = 546$	
Dimensions (cm)	84×42	44×34	
Weight (kg)	2	1	
Retro-reflec. mirrors	—	1 mm thick plane glass	
PMTs ($\varnothing$ (in))			Hamamatsu R1332Q - 2″
Number of PMTs	8	8	
Radiator length (cm)	93–72[a]	34–39	
Light collection efficiency	0.84–0.90[a]	0.84–0.98	0.75–0.88

The ordering or the radiator length values corresponds to that of the angles.
[a] These values refer to $15^\circ < \theta < 34^\circ$; in the region $34^\circ < \theta < 38^\circ$ the radiator length varies from 39 to 29 cm and the light collection efficiency is < 0.70.

shows the reflectance as a function of wavelength for two typical mirrors. The plexiglass substrates and glass substrates perform equally well for wavelengths above 200 nm.

5.5.3. Performance of the Cherenkov counter

All PM signals are directly amplified by a factor $\simeq 10$. Each output is split in two, one half sent to the trigger logic and the other to an ADC to record the integrated charge. We describe the following aspects of counter performance:

1. fast logic trigger efficiency, which is affected by the light yield by the azimuthal cracks and septum;
2. light yield: number of p.e. as a function of θ and ϕ;
3. light yield: comparison of Freon 13 and Freon 12;
4. counter aging.

5.5.3.1. Cherenkov counter efficiency. As described in Section 6, the basic trigger requires

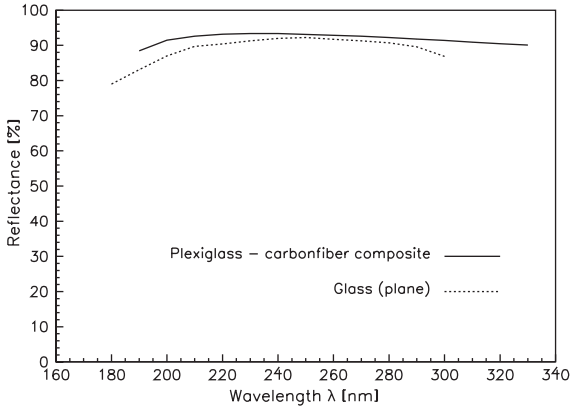

Fig. 17. Reflectance of plane (dotted) and ellipsoidal (solid) mirrors as a function of the light wave length.

two charged particles, at least one tagged as an electron candidate by a signal from the corresponding Cherenkov section.[10] Independently, two large energy depositions in the central electromagnetic calorimeter, separated by more than 90° in azimuth, are also required as a signature of the decay of a high mass object. To evaluate the Cherenkov counter efficiency we select two samples of events identified as:

$$\bar{p}p \to J/\psi \to e^+e^- \tag{12}$$

or

$$\bar{p}p \to \chi_2 \to J/\psi\gamma \to e^+e^-\gamma. \tag{13}$$

This selection uses the basic electron trigger (see Section 6), logical branch *one electron*, where the minimum requirement is one Cherenkov signal above threshold. No further use of the Cherenkov signals is made in the offline selection; an event is accepted if it satisfies a kinematical fit (4 or 5 constraints respectively) with a probability greater than 1%. For reaction (13) the γ is required to be detected by the lead-glass calorimeter. Using off-resonance data, we determine the background in these samples to be 0.03% and 1.3% respectively.

[10] In principle, this introduces a bias in the study since the trigger rejects events where both electrons give no signal in the Cherenkov counter. However the probability of this occurrence is $(2.2 \pm 0.8)\%$, small enough to not affect any of our conclusions.

To determine the Cherenkov efficiency we compare the numbers of events with (1e) at least one of the tracks tagged as an electron, with (2e) with both electrons tagged. For the latter, we apply a further cut $|\Delta t| \leqslant 10$ ns, corresponding roughly to 3σ, to ensure that both electrons come from the same event. From the ratio $r = 2e/1e$ for 443 events of reaction (13), we compute the detection probability for a single electron as $\varepsilon = 2r/(1+r) = 98.1 \pm 0.5$. Reaction (12) gives fully compatible results.

5.5.3.2. Performance with CO_2 and Freon 13. To measure the average number of p.e. per electron track we select a clean sample of charmonium events corresponding to reactions (12) and (13). The selection is again based on a standard kinematical fit, topological consistency, with no requirements on the Cherenkov signals. We use the Cherenkov signal charge distribution to estimate the light yield. The average charge can be converted to an average number of p.e. provided one knows the PM gain for the conditions of operation or, equivalently, the number of ADC counts per p.e. We determine the latter by measuring the pedestal and dark current ADC spectrum for each PM; the separation between the dark current peak and the pedestal corresponds to one p.e. These measurements were frequently repeated during data taking.

The p.e. distributions in given θ intervals for an ellipsoidal and a spherical mirror are shown in Fig. 18. The curves represent Poisson fits, where the mean is a free parameter.

The average number of p.e. is reported, for several intervals of θ (integrated over ϕ), in Table 3 (ellipsoidal) and Table 4 (spherical). These data were taken at the beginning of the experiment. For comparison, the second line of each table reports the expected number of p.e. calculated from a Monte-Carlo simulation [23]. The experiment finds substantially fewer p.e. than the Monte Carlo and this discrepancy has not been explained.[11] We observe that in the septum region the light yield is roughly at the same level as that of

[11] Other experiments using the same or similar photomultipliers have observed a similar effect [22,24].

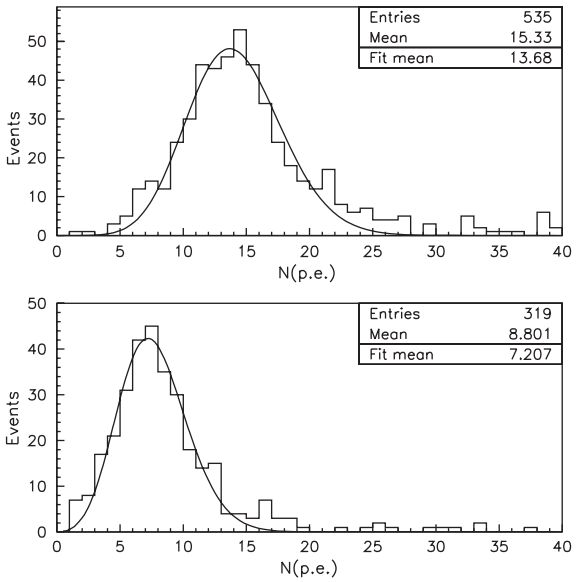

Fig. 18. Distribution of the number of p.e.per electron track: (top) for an ellipsoidal mirror in the interval $24^\circ < \theta < 28^\circ$, (bottom) for a spherical mirror in the interval $40^\circ < \theta < 44^\circ$.

the neighboring θ regions. This is achieved by means of the overlap of the two cells in the interval $34^\circ < \theta < 38^\circ$: here the two signals are summed offline and, although the small angle cell typically contributes only 1.5 p.e., this technique is very effective in making the counter performance smooth over the septum region.

In Fig. 19 the measured number of p.e., averaged over the 8 mirrors in each cell, is plotted as a function of θ. Finally, the light yield of an ellipsoidal mirror integrated over θ from 15° to 34° is plotted in Fig. 19b as a function of ϕ. Again the uniformity is satisfactory and only for the last few degrees of both mirror edges is there a significant light loss which, however, does not significantly diminish the overall efficiency of the detector.

5.5.3.3. Performance with CO_2 and Freon 12. During the last month of the 1996/1997 run and the entire 2000 data taking, Freon 13 was used instead of Freon 12 in the large angle cell. The average number of p.e. for a sample of 1360 electrons from χ_1 and χ_2 events, integrated over ϕ and over θ from 34° to 65°, is 9.50 ± 0.13, to be compared with 8.30 ± 0.11 from a sample of 1770 electrons in Freon 13 from J/ψ formation and decay.[12]

The light yield of the detector using Freon 12 is consistent with that using Freon 13 after accounting for the difference in $\sin^2\theta_c$ (1.5), the relative transmittance (0.86), and the relative collection efficiency (0.90).

5.5.3.4. Counter aging. During 1996–97 data taking, which spanned almost a year, we observed a continuous decrease of the counter signal size, about 13% in both cells. The effect cannot be attributed to PM gains, which were monitored through periodic measurements of the dark current pulse-height spectrum, and were found to be constant to within $\pm 3\%$. Also, reflectance measurements performed at the end of data taking gave results very close to those obtained before mirror installation. However PM quantum efficiencies were not monitored.

While for the large θ cell we have not found an explanation for the effect, measurements of the curvature of the ellipsoidal mirrors (small θ cell), performed approximately one and a half years after the end of data taking, showed a significant deformation of the substrates, largely accounting for the signal-size decrease.[13]

The pattern of the deformation for the elliptical mirrors is similar for all eight cells: a decrease of curvature in the longitudinal cross-section and an increase in the transverse cross-section. The sagittas changed by as much as 5 mm. The probable cause of the deformation is a relaxation of the carbon fiber structure. This experience indicates that for complex mirror shapes that contain a large range of radii of curvature, a simple carbon-fiber substrate of constant thickness with no extra reinforcement is inadequate. Solutions such as honeycomb [25] or fins may be suitable, but their long term stability should be carefully tested. For the use of this counter in the year 2000 run, we tested and adopted the following

[12] The Freon 13 data we refer to were collected five weeks before the Freon 12 data.

[13] We do not know the time development of this deformation. Monte Carlo simulations of the performance of the mirrors in their deformed shape indicate a loss exceeding the observed 13%.

Table 3
Average number of p.e. per electron track in the small θ cell (elliptical mirrors) of the Cherenkov detector at different θ intervals: Monte Carlo simulations are also reported

θ (deg.)	15–20		20–24		24–28	28–32		32–34
$\langle n_{pe} \rangle$ exper.	19.8 ± 2.3		18.3 ± 1.3		17.2 ± 2.1	14.8 ± 1.2		11.8 ± 1.1
θ (deg.)	15–18	18–20	20–22	22–24	24–28	28–30	30–32	32–34
$\langle n_{pe} \rangle$ M.C.	20.6	22.5	22.4	21.2	20.2	19.3	18.1	16.5
ε_{geom}	0.83	0.90	0.90	0.90	0.90	0.90	0.90	0.86
L (cm)	93.1	95.1	94.	88.8	85.	80.8	76.5	72.1

Table 4
The same as in Table 3 for the large θ cell (spherical mirrors)

θ (deg.)	34–38	38–42	42–46	46–50	50–54	54–58	58–65
$\langle n_{pe} \rangle$ exper.	8.2 ± 1.6	8.7 ± 1.7	9.3 ± 1.6	9.7 ± 1.7	9.8 ± 1.7	8.3 ± 0.9	6.8 ± 1.1
θ (deg.)	34–38	38–42	42–46	46–50	50–54	54–60	60–65
$\langle n_{pe} \rangle$ M.C.	12.7	14.1	14.6	15.0	15.2	15.5	14.9
ε_{geom}	0.91	0.97	0.97	0.97	0.97	0.97	0.93
L (cm)	34.2	35.6	36.8	37.7	38.4	39.0	39.1

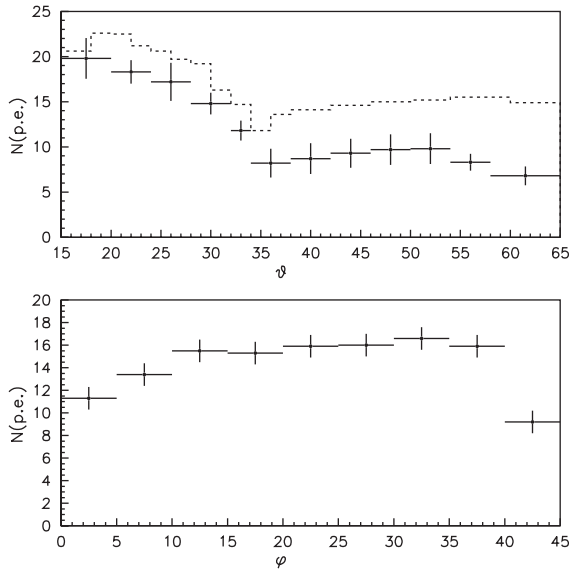

Fig. 19. (upper) Average number of p.e. versus θ. The dashed line shows the number expected from the MC (see text). (lower) Average number of p.e. versus ϕ for an elliptical mirror.

simple solution; a single steel cable (1 mm diameter) was mounted on the longitudinal axis of each substrate: since the deformation is quite symmetrical with respect to the long axis of the ellipsoid, we were able to retrieve the original shape of the substrate both transversely and longitudinally by adjusting the cable tension. This adjustment was monitored with templates and later checked with ray tracing.

5.6. The central calorimeter

The central calorimeter (CCAL) [26–28] is a cylindrical array of 1280 Schott F2 lead-glass Cherenkov counters. It measures the energy and position of electromagnetic showers. The lead glass characteristics are given in Table 5.

Each counter points toward the interaction region in a projective geometry. A *ring* in θ contains 64 counters, and a *wedge* in ϕ contains 20 counters. Fig. 20 is a slice of the CCAL in ϕ, showing the layout of the counters of two wedges. Each wedge is contained in a light-tight stainless-steel container with exterior surfaces 0.735 mm thick and separators between counters 0.254 mm thick. Thus the material separating counters in adjacent wedges is about six times greater than that separating counters within wedges. In the azimuthal (polar) direction 2% (0.5%) of the surface is inactive.

The photomultipliers are chosen for efficient photoelectron collection rather than fast timing and for relative insensitivity to magnetic fields, since in this geometry good magnetic shielding is

Table 5
Properties of the Schott F2 lead glass used in the Central Calorimeter

Radiation length	3.141 cm
Density	3.61 g cm^{-3}
Refractive index at 404.7 nm	1.651
Composition by weight:	
Lead	42.2%
Oxygen	29.5%
Silicon	21.4%
Potassium	4.2%
Sodium	2.3%
Arsenic	0.15%
Transmittance through 10 cm	
Wavelength (nm)	Transmittance (%)
335–344	56.9
385–394	95.5
435–444	97.9
485–494	98.4
535–544	98.9
585–594	99.4

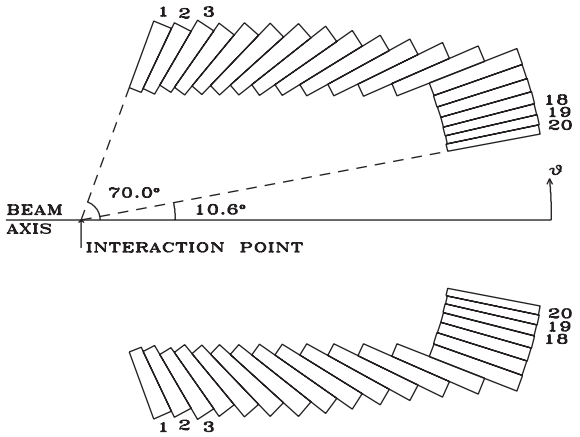

Fig. 20. The geometry of the counters in two wedges of the central calorimeter.

difficult to achieve. Four PM diameters are used to maximize the photocathode coverage.

The CCAL coverage in θ is constrained in the backward (large θ) region by the physical presence of the gas-jet pumping system and in the forward region (small θ) by the increasing radiation dose the glass sees during running, as well as the decreasing rate for charmonium events

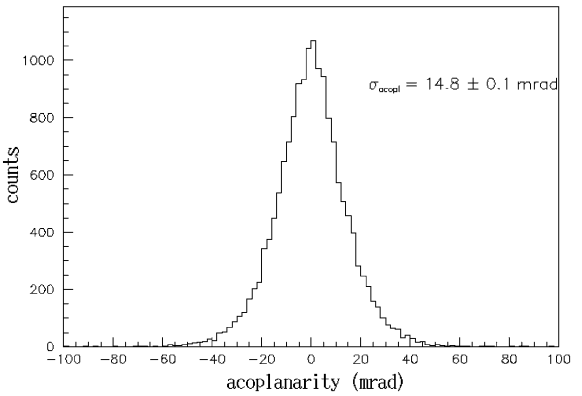

Fig. 21. Acoplanarity ($\Delta\phi$) distribution for clean $J/\psi \to e^+e^-$ decays.

compared to that for forward-peaked hadronic background.

5.6.1. Energy and position resolutions

We compare the energy and angular resolutions of the CCAL with those measured by E760, namely, an average rms position resolution [29] of 9 mm, corresponding to ϕ and θ angular resolutions of $\sigma_\phi = 11$ mrad and $\sigma_\theta = 6$ mrad respectively, and an energy resolution approximated by

$$\frac{\sigma(E)}{E} = \frac{6.0\%}{\sqrt{E(\mathrm{GeV})}} + 1.4\%. \quad (14)$$

We measure the angular resolution using a clean sample of e^+e^- from J/ψ decays, selected using the hodoscopes and the Cherenkov counter. The quantity $\Delta\phi \equiv \pi - |\phi_1 - \phi_2|$ measures the deviation from coplanarity. We expect $\sigma_{\Delta\phi} = \sqrt{2}\sigma_\phi = 15.6$ mrad. The distribution of $\Delta\phi$ is shown in Fig. 21, with $\sigma_{\Delta\phi} = 14.8$ mrad. We consider the quantity $\Delta\theta = \theta_{1,\mathrm{pred}} - \theta_{1,\mathrm{meas}}$, where $\theta_{1,\mathrm{pred}}$ is calculated from $\theta_{2,\mathrm{meas}}$, assuming two-body kinematics. The expected value for $\sigma_{\Delta\theta}$ is a function of θ, shown in Fig. 22 for $\sigma_\theta = 6$ mrad, together with the $\sigma_{\Delta\theta}$ of the e^+e^- data. The angular resolution is consistent with that measured in E760.

The energy resolution is measured using $J/\psi \to e^+e^-$ events, where one can predict the energy of each electron from its direction. Fig. 23

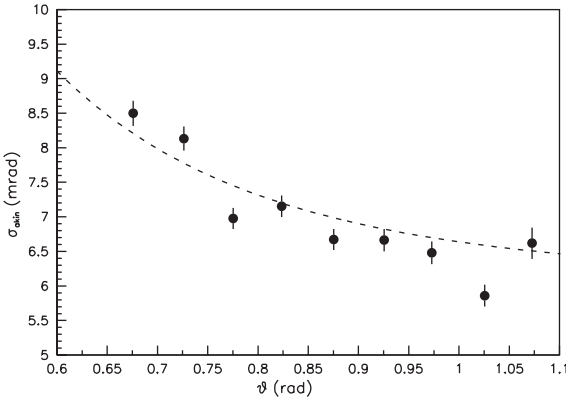

Fig. 22. Akinematics ($\Delta\theta$) standard deviation as a function of θ for clean $J/\psi \to e^+e^-$ decays. The curve indicates the expected $\sigma_{\Delta\theta}$ for a resolution $\sigma_\theta = 6$ mrad.

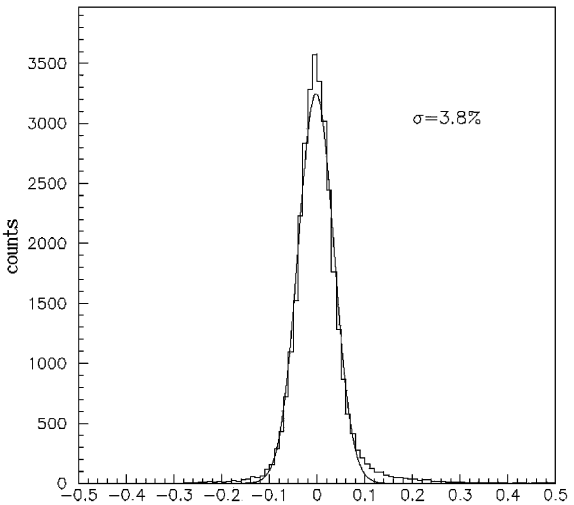

Fig. 23. Distribution of the difference between predicted and measured CCAL energy divided by the measured value. Its width confirms the validity of Eq. (14).

shows the distribution of $(E_{\text{meas}} - E_{\text{pred}})/E_{\text{pred}}$, which has σ in agreement with Eq. (14).

5.6.2. The monitoring system

For monitoring and testing purposes, a network of plastic-polymer optical fibers transmits light to the back of each lead glass block. The xenon flash lamp used in E760 was replaced with a nitrogen laser for E835. The laser produces 3 ns-wide pulses with wavelength 337.1 nm which are directed to a

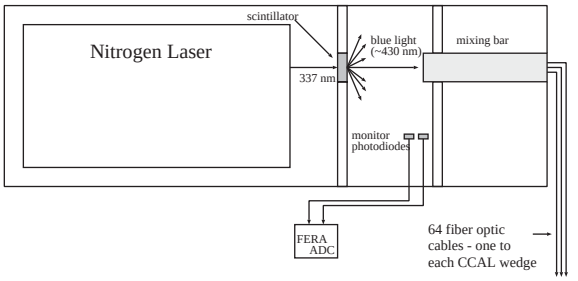

Fig. 24. Layout of the aluminum laser box containing the laser, the scintillator, and the major mixing bar.

scintillator that produces light at $\sim$430 nm, a wavelength which is transmitted efficiently by the fibers. The scintillation light is passed to a rectangular lucite mixing bar and distributed to optical fibers coupled to the lucite, one (plus spares) directed to each wedge of the CCAL. Within the wedge container, the light encounters a secondary mixing bar which further distributes the light to 20 more fibers, one coupled to the back of each counter. A light-tight aluminum box holds the laser, the scintillator, the major mixing bar and two PIN diodes, used to measure the intensity of the laser pulse, as shown in Fig. 24. This system was indispensable for testing the CCAL counters, prior to and during the data taking, and was also used to monitor the gain of the counters. The calibration method is described in Section 8.3.

5.6.3. Readout electronics

The signals from the calorimeter first pass to a *summer box* (see Section 6.2) where 5% is tapped for triggering purposes. The remaining signal passes through 310 ns of RG-58 delay cable allowing time for the trigger decision to be made before the signal reaches the readout electronics. The cable disperses and attenuates the signal, extending the pulse tails to over 600 ns. In E760, the luminosity was such that the pulse tails from earlier interactions appeared as extra clusters in a few per cent of events. For the increased rate of E835, this contamination would have been detrimental to the data quality, especially for the $\gamma\gamma$ final states.

We added an active filter to reshape the pulses from the CCAL and provide a logic pulse for

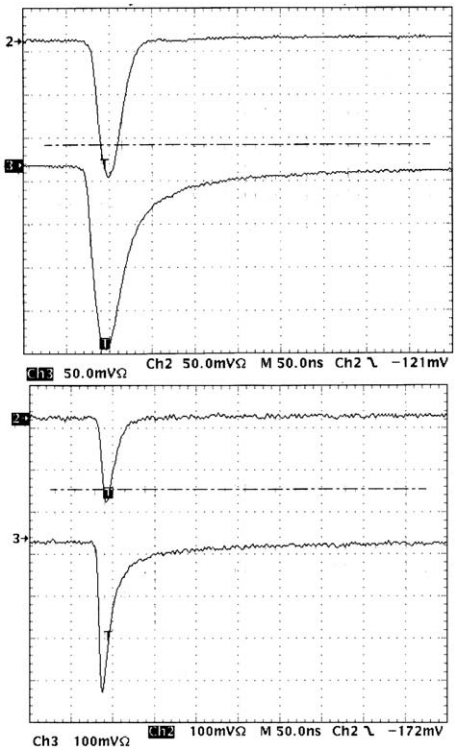

Fig. 25. Oscilloscope trace showing the input (lower trace in each plot) and output (upper trace) of the shaper circuit for a 1 GeV pulse from a 3-in. PMT in ring 10 (up) and a 2-in. PMT in ring 17 (down). The pulses are from beam interactions, with the same electronics chain used during data taking. Horizontal scale is 50 ns/div in both pictures. Upper traces have vertical scale at 50 mV/div; lower ones have 100 mV/div.

timing purposes. There are three versions of the shaper circuit, for rings 1–16, 17–18 and 19–20, since the PMT electronics is different, yielding different signal shapes. Fig. 25 displays oscilloscope traces of the input and the shaper output for the first two of these. Each shaper circuit board has 16 channels; the diagram for a single channel is shown in Fig. 26. The circuit replaces a simple voltage divider with a gain of 0.5 used in E760 at the input to the ADC. Two voltage dividers set the overall gain of the shaper circuit equivalent to that of E760. By narrowing the pulses, the same amount of charge is collected in a 100 ns ADC gate as E760 collected in 150 ns. The improvements in both gate length and pulse shape allow E835 to operate at three times the instantaneous luminosity of E760 with the same fraction of contaminated events. The addition of timing information allows most of the contamination to be identified and separated from the triggering event (see Section 8.3).

5.7. The forward calorimeter

The forward calorimeter [30] used in E760 was replaced in April 1997 with one built from existing lead-glass counters. This detector is an array of rectangular SF2 lead-glass blocks, each viewed by a PM glued to one end of the block; the characteristics are summarized in Table 6. The small and large blocks had been previously glued to PMs. The medium blocks were glued with Epotek-302, a radiation-resistant optically-clear epoxy.

Since the available lead glass blocks were not equal in size, an irregular grid (see Fig. 27) was devised to cover the required acceptance, and achieve an adequate overlap with the Central Calorimeter. The characteristics of the blocks are found in Table 7.

The readout of the new FCAL is the same as for the CCAL. The PM signals are shaped by similar boards, with gains and time constants matched to the signals of the FCA PMs. During 1996/1997 run the shapers for the small and medium blocks have $\times 2$ gains, while the shaper for the 16 large blocks has a $\times 1$ gain. In run 2000 a single shaper board type was used for all FCAL blocks.

To obtain an initial calibration, each block was placed in a muon beam downstream of the Fermilab MTEST area. For every block, the high voltage was adjusted so that the signals from through-going muons, measured using a LRS QVT and weighted by the block's length, were equal.

5.7.1. FCAL calibration

Six-photon events at the χ_1 energy are used to calibrate the FCAL. Five photons are required to be in the CCAL, and one in the FCAL. Two pairs of CCAL clusters are required to form an invariant mass consistent with either a π^0 or an η. The remaining CCAL cluster is paired with the FCAL cluster; without using the FCAL cluster

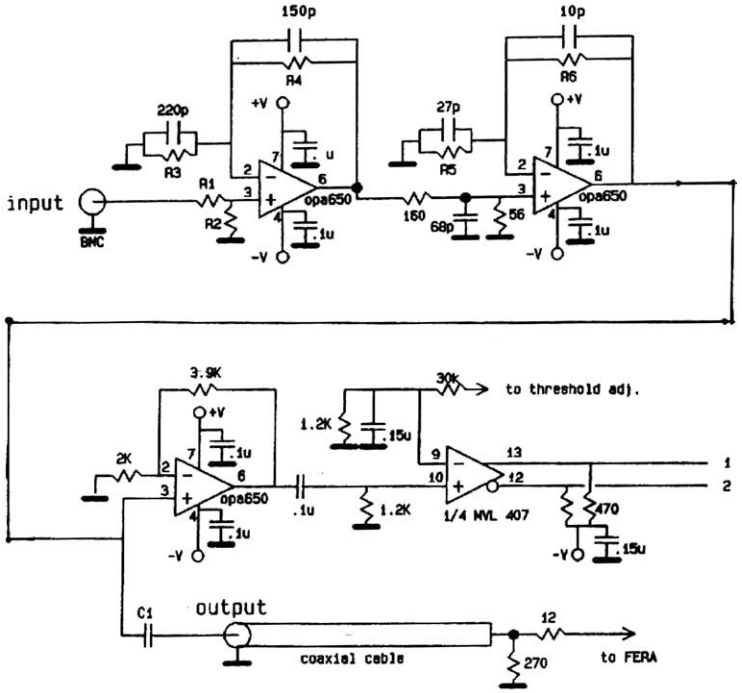

Tube diameter		R1	R2	R3	R4	R5	R6	C1
(3")	1	24	27	1.2K	1.0K	1.3K	1.3K	22nF
(2")	2	30	20	1.2K	680	820	1.5K	22nF
(1.5")	3	30	18	910	680	680	1.5K	18nF

Fig. 26. A circuit diagram of the shaper board that is used to filter out the CCAL signal tail. Only one of the 16 channels is shown, along with the potentiometer that controls the discriminator threshold for all 16 channels and the power connection. Different versions of the circuit are used for rings 1–16, 17–18 and 19–20 since the smaller PMTs (rings 17–20) have different pulse shapes. The component values used for each version are given in the table. The Forward Calorimeter required its own shaper boards because of the different shape of the signal.

Table 6
Geometrical and physical parameter of the forward lead-glass electromagnetic calorimeter

Material	SF2 lead glass ($n = 1.673, L_{\mathrm{Rad}} = 2.76$ cm)
Structure	144 variable size rectangular blocks
Geometrical acceptance	3.3°–11.0°
Thickness	13–21 radiation lengths

energy, SQUAW is used to fit the hypotheses $\pi^0\pi^0\pi^0$, $\eta\pi^0\pi^0$ and $\eta\eta\pi^0$. Fig. 28 shows the invariant mass distribution of the CCAL-FCAL pairs for events that fit one of these hypotheses. The π^0 peak is mainly due to events with FCAL energies less than 250 MeV, and the η peak is mainly derived from events with FCAL energies above 500 MeV.

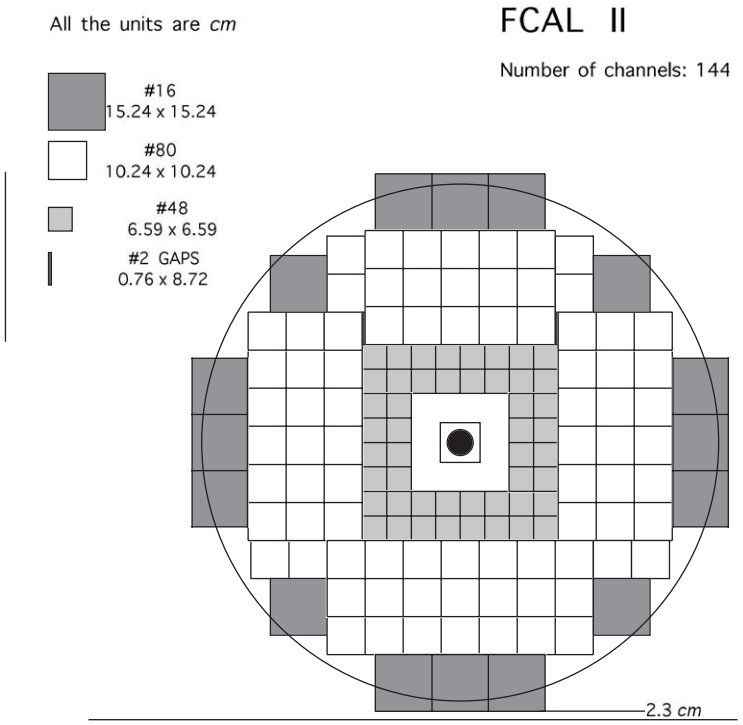

Fig. 27. Schematic block layout of the forward lead glass calorimeter.

Table 7
Summary of the block characteristics of the forward lead-glass electromagnetic calorimeter

	Size (cm)		L_R	Wrapping	PM type
	Cross s.	Length			(RCA)
48 "small"	6.3×6.3	58.6	21	Al foil/Tyvek	6342A ($2\frac{1}{2}''$)
80 "medium"	10×10	38	14	Al foil/Tyvek	6342A ($2\frac{1}{2}''$)
16 "large"	15×15	36	13	Alum. PVC	4335 ($5''$)

5.8. The luminosity monitor

As discussed above, excitation function measurements require accurate normalization of each data point with respect to its integrated luminosity. It was therefore necessary to design a $\bar{p}p$ luminosity monitor which could measure relative luminosity to better than 1%, and absolute luminosity with an uncertainty of $\sim 2\%$.

The E760/E835 luminosity monitor is based on making absolute measurements of $\bar{p}p$ elastic scattering differential cross-sections at extreme forward angles by measuring recoil protons as close as possible to the limiting angle $\theta = 90^\circ$, or $\alpha \equiv 90 - \theta = 0^\circ$.

The squared momentum transfers, $|t|$, for these measurements are as small as $|t| = 0.0005$ $(\mathrm{GeV}/c)^2$. This typically corresponds to θ (scattered $\bar{p}$) $= 0.20^\circ$, where it is very difficult to make measurements, and to θ (recoil proton) $= 89.2^\circ$, where recoil protons can be conveniently detected. At these very small momentum transfers elastic

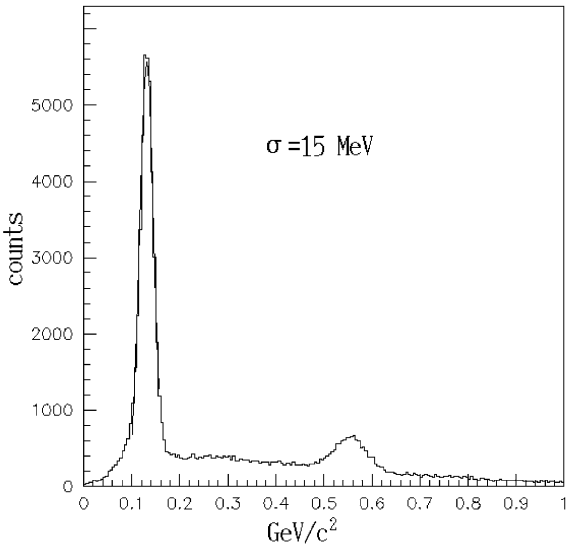

Fig. 28. Two photon invariant mass for paired clusters in the FCAL and CCAL. The π^0 peak is fitted with a Gaussian.

scattering is overwhelmingly Coulombic ($\approx 95\%$ at $|t| = 0.0005$ $(\mathrm{GeV}/c)^2$), allowing accurate absolute normalization. Another important advantage is that since the recoil proton energies are only a few MeV (for $\alpha \leqslant 6^\circ$, $T(p) \leqslant 15$ MeV for the highest $\bar{p}$ energies used in our charmonium measurements), they can be detected in solid state detectors of excellent energy resolution and stability.

The luminosity $\mathscr{L}$ is related to the measured recoil rate N in a detector which subtends a solid angle $d\Omega$ as

$$\mathscr{L} = N/[(d\sigma/dt)(dt/d\Omega)\, d\Omega]. \tag{15}$$

The differential cross-section is,

$$d\sigma/dt = |F_c(t)e^{i\delta} + F_n(t)|^2. \tag{16}$$

The Coulomb amplitude $F_c(t)$ and phase δ are exactly calculable. The nuclear amplitude is

$$F_n(t) = \sigma_T(\rho + i)e^{-b|t|/2}/\left(4\sqrt{\pi}\hbar\right). \tag{17}$$

Thus, in order to determine absolute luminosity via Eq. (15), the three parameters, the total cross-section σ_T, the 'slope' parameter b of forward nuclear scattering, and the parameter $\rho \equiv \mathrm{Re}\, f(0)/\mathrm{Im}\, f(0)$, must be determined.

The E760/E835 luminosity monitor is designed for the dual purpose of measuring σ_T, b, and ρ for $\bar{p}p$ elastic scattering in the energy region of interest, and, by using them, to provide an absolute luminosity for the charmonium measurements. The original design of the E760 luminosity monitor has been described in detail earlier [31]. Its assembly is schematically illustrated in Fig. 29. In Fig. 29 we also show the design of the detector assembly as revised for E835.

The luminosity monitor consists of a conical vacuum enclosure (horn) suspended just below the $\bar{p}p$ interaction region at 90° to the $\bar{p}$ beam. At its bottom there is a pan containing an assembly of five solid state detectors on a carriage, which can be moved parallel to the beam from outside, one solid state detector at fixed recoil angle $\alpha = 3.547 \pm 0.006^\circ$ during the E760 measurements, and left and right fixed detectors at $\alpha_L = 3.496 \pm 0.005^\circ$ and $\alpha_R = 3.511 \pm 0.005^\circ$ during the E835 measurements.

The detectors are silicon surface barrier (500 μm deep) and Si-Li drift (3000 μm deep) of area ≈ 1 cm × 5 cm each, deployed according to the expected maximum recoil energy expected at different recoil angles. The carriage can be moved such that the detectors can sample all recoil energies, from $\alpha = 0^\circ$ to 6°. A typical recoil spectrum is shown in Fig. 30. It is seen that the smooth background occurs at the level of ~2–4% of the recoil peak, and that it can be subtracted reliably. Typical count rates in the detectors during data taking are 10–20 Hz.

The detectors are regularly calibrated with a ^{244}Cm alpha source, which is inserted pneumatically. The typical energy resolution of the detectors is ~40 keV for 5.742 MeV alphas. Before the pan assembly was attached to the luminosity monitor horn, the surface area of each detector was determined by mounting a calibrated ($\pm 0.4\%$) ^{241}Am alpha source supplied by the National Bureau of Standards. The solid angles subtended by the detectors were determined by surveying the distance (149.60 ± 0.03 cm) between the effective $\bar{p}p$ interaction point and the detector surfaces. We found that the best determination of the recoil angle ($\pm 0.006^\circ$) is obtained from the centroid of the recoil peak.

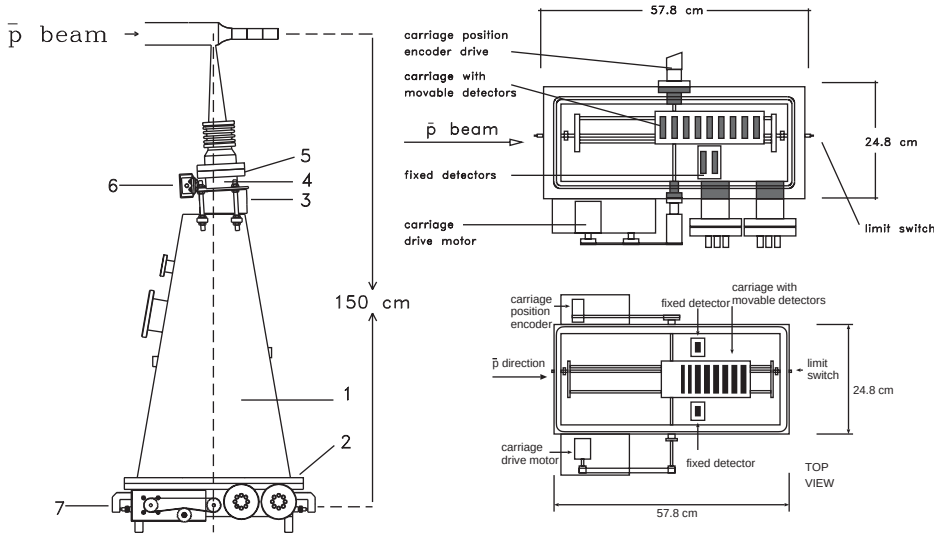

Fig. 29. Schematic of the Luminosity Monitor. Left: assembly view; top right: the detector pan as used in E760; bottom right: the detector pan as used in E835.

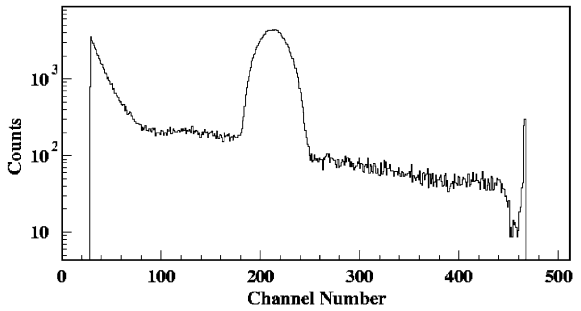

Fig. 30. Example of the proton recoil spectrum obtained with one of the detectors during E835.

During E760, forward scattering data were taken with the movable detectors at antiproton momenta corresponding to all the charmonium resonances studied. The resulting differential cross sections are shown in Fig. 31. Analysis of these cross-sections led to the determination of σ_T, b, and ρ parameters at various antiproton momenta [32]. These were fitted to smooth curves, leading to the local (valid for lab momentum $p = 2$–8 GeV/c) parametrization as follows

$$\sigma_T(\text{mb}) = 34.48 + 89.7p^{-0.70} \tag{18}$$

$$b((\text{GeV}/c)^{-2}) = 13.64 - 0.2p \tag{19}$$

$$\rho = -0.12 + 0.03p. \tag{20}$$

These parameters are used to calculate $d\sigma/dt$ for any beam momentum at momentum transfer squared, $|t|$, corresponding to the fixed detector. Luminosity is determined according to Eq. (15). Both instantaneous luminosity (integrated over 2 min) and integrated luminosity (integrated over a whole run extending over several hours) are monitored. The statistical errors in integrated luminosity are $\leqslant 0.3\%$. The systematic error in integrated luminosity is estimated as $\sim 2.1\%$, arising mostly from the uncertainties in the parametrization of Eq. (20).

During the E760 running we found that the antiproton orbit could occasionally undergo radial shifts of several mm. These shifts lead to errors in the luminosity due to shadowing of the intersection volume by the aperture at the entrance to the luminosity monitor horn. We redesigned the luminosity monitor pan and provided two fixed detectors, one on each side of the movable detector carriage. The modified design, used for monitoring in E835, is shown in Fig. 29(c). Displacement of the beam from the central orbit causes asymmetry in the counts in the two fixed detectors. For orbit displacements of magnitude <1.5 mm, the asymmetry $(L - R)/(L + R)$ is calculated to be less than

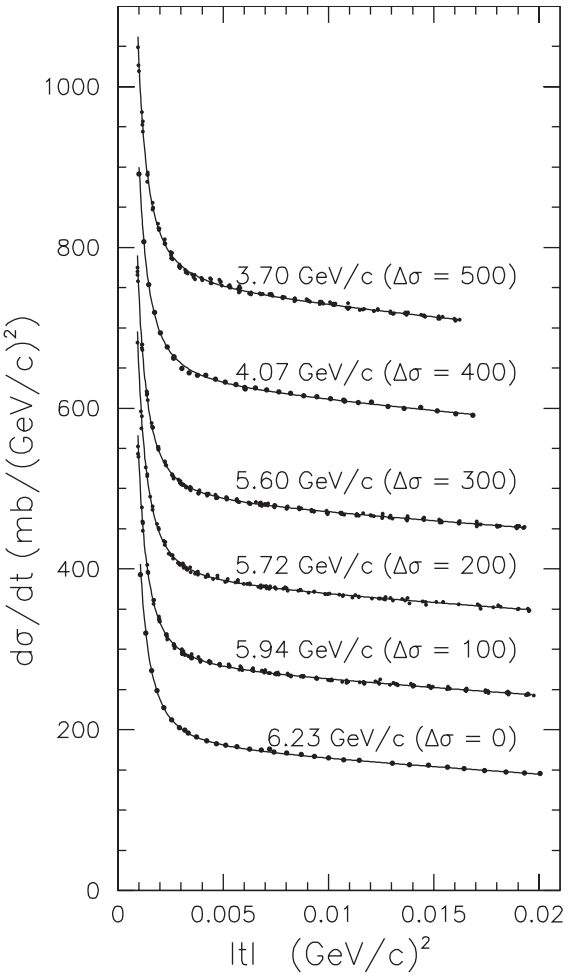

Fig. 31. The measured differential cross-sections (increased as indicated by amounts $\Delta\sigma$ (mb/(GeV/c)^2) for display purposes) for six beam momenta. The solid lines represent fits to the data.

2%, and no corrections were applied to the average luminosity. For displacements of magnitude >1.5 mm, but <3.0 mm, corrections are calculated to be $<10\%$. However, whenever the asymmetry is larger than 2%, we adjust the beam orbit to its central value.

6. The trigger system

The triggers for charged and all-neutral final states are formed independently and fanned into a final trigger stage along with the random trigger used for collecting events for studying accidentals with the simulation.

6.1. Charmonium charged final states

The charged trigger [33] is designed mainly to select the electromagnetic decays of charmonium states, e.g., $\bar{p}p\to J/\psi\to e^+e^-$ or $\bar{p}p\to\chi_{1,2}\to J/\psi+\gamma\to e^+e^-\gamma$.

The only hadronic channel that is selected is two ϕ mesons: $\bar{p}p\to(\bar{c}c)\to\phi\phi\to 4K^\pm$. It may be possible to study the $^1S_0$ states of charmonium,[14] i.e., the η_c and η_c', in this reaction. In this case the first level trigger uses the informations from the inner tracking system only.

The charged trigger selects events with one or two electron tracks, one or two charged tracks; $\phi\phi$, and generates a neutral veto. The input signals are the outputs of the hodoscopes H1, H2, H2′, of the Cherenkov counter and of the scintillating fiber detector. The selection of e^+e^- events, both exclusive and inclusive, is based mainly on the Cherenkov counter signals. The scintillating fiber detector plays the crucial role in the selection of $\phi\phi\to 4K^\pm$ events. The expected cross-section $\sigma_{\phi\phi}$ is about 2 nb, while the total cross-section for $\bar{p}p\to 4$*prongs* is 22 mb. Since we do not identify kaons, we rely upon the scintillating fiber detector for the θ information required for kinematical selection of this channel with sufficient rejection power and acceptable efficiency (see Table 8). In Fig. 32 the most important angular distributions of the $\phi\phi\to 4K^\pm$ reaction are shown.

The hardware of the charged trigger consists of CAMAC and NIM modules. In Fig. 33 a schematic of the trigger is shown. It is divided into three successive stages: the discrimination stage, the single logic stage and the final trigger stage. In the first stage, the signals from the hodoscopes, the Cherenkov, and the scintillating fiber detector are discriminated. For the hodoscopes and the Cherenkov, the discrimination is performed by six LRS 4413 discriminators. All 80 discriminated signals go to the trigger logic and to TDCs.

[14] The $^1P_1$ may also be studied through the decay $^1P_1\to\eta_c\gamma\to\phi\phi\gamma$.

Table 8
Efficiency and stability of the charged trigger logic

Charged trigger efficiency			
	e^+e^-	$e^+e^-\pi^+\pi^-$	$e^+e^- + \gamma s$
ε (%)	90 ± 1	86 ± 1	89 ± 1
$\phi\phi$ *trigger efficiency*			
	$\phi\phi(\eta_c)$	$\phi\phi(\eta_c')$	
ε (%)	51 ± 5	48 ± 5	
Charged trigger stability			
C_MLU1	3.8%	2.7%	3.4%
C_MLU2	3.0%	3.0%	3.0%
ϕ_MLU1	12.8%	10.2%	9.7%

Trigger efficiencies are measured for both exclusive and inclusive e^+e^- events. $\phi\phi$ efficiencies strongly depend on energy. The apparent poor stability of the $\phi\phi$ trigger is due to its strong energy dependence. The quoted numbers refer to 1996/1997 run.

The discrimination of the signals from the outer scintillating fiber detector is done with 32 discri-or modules. Each discri-or accepts inputs from 32 fibers and produces 32 signals for digital readout, 32 signals for analog readout, and the OR of all its inputs. For bundles with 32 or fewer fibers, signals (see Fig. 34) are sent to a single discri-or module. For bundles with more than 32 fibers, the inner and outer fibers are sent to different discri-or modules and the OR outputs OR-ed. The total number of OR signals is then 19, the number of fiber bundles, and these are used in the $\phi\phi$ trigger.

The second stage of the charged trigger consists of the *single-logic* modules. These are:

- track reconstruction;
- multiplicity;
- coplanarity;
- neutral veto;
- forward veto;
- $\phi\phi$ logic.

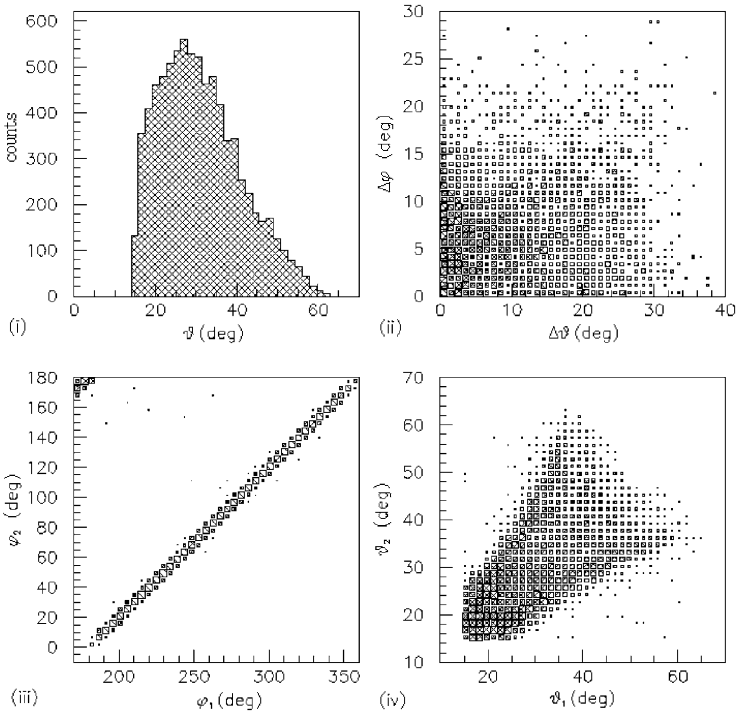

Fig. 32. Kinematical features of the reaction $\bar{p}p \to \eta_c \to \phi\phi \to 4K^{\pm}$. (i) θ distributions of the kaons; (ii) opening angles of kaons from the same ϕ meson; (iii) correlation between the azimuthal angles of kaons coming from different ϕ mesons; (iv) correlation between the polar angles of kaons from the same ϕ meson.

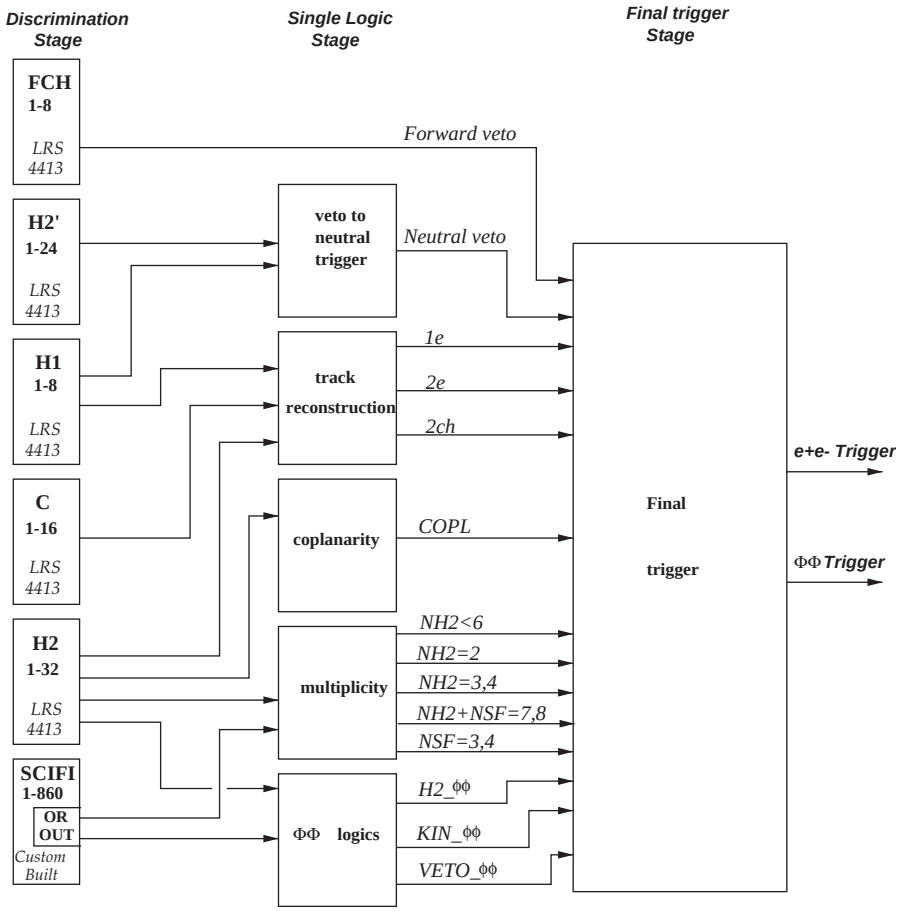

Fig. 33. General scheme of the charged trigger layout.

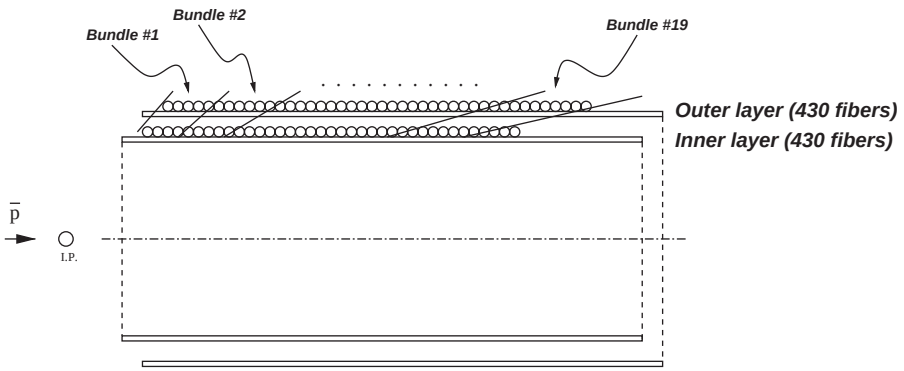

Fig. 34. Schematic view of the polar angle coverage of the scintillating-fiber bundles used in the $\phi\phi$ trigger. The interaction point (I.P.) is at the left of the figure.

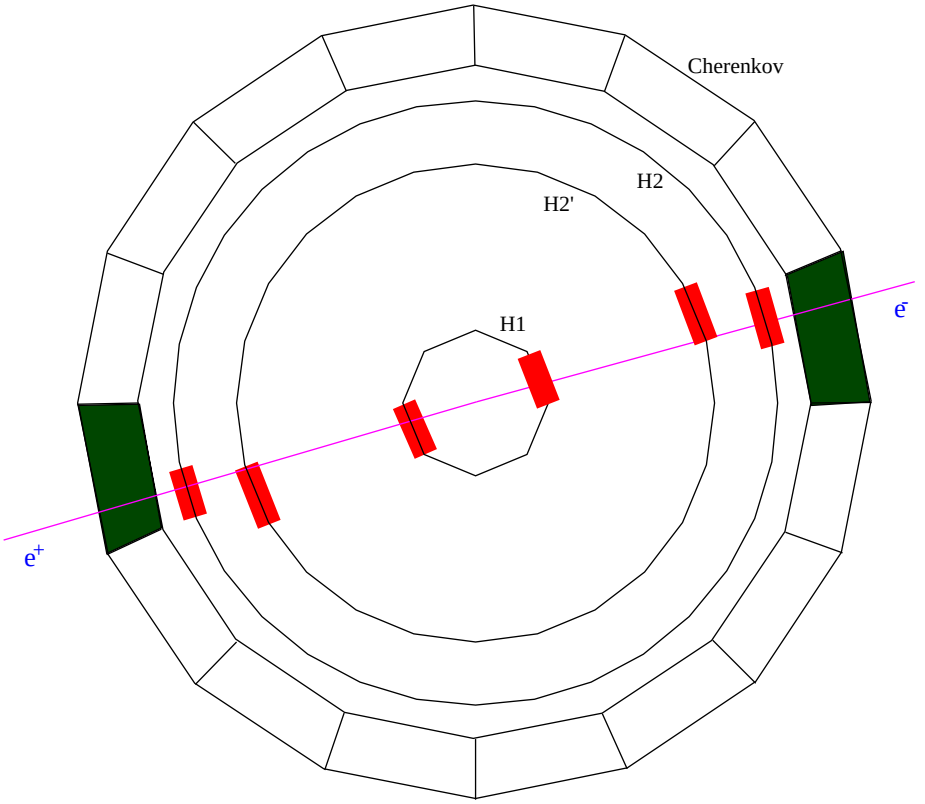

Fig. 35. Topology of a two body event as seen by the charged trigger. A charged particle is defined as a coincidence of corresponding modules in H1 and H2; an electron is defined as a charged particle with an associated Cherenkov signal.

The track reconstruction module gives the number of *charged tracks* and number of *electrons*. A charged track is defined as the coincidence between one element of H1 and a corresponding element of H2 as shown in Fig. 35. An *electron* is a charged track where the coincidence with the corresponding Cherenkov octant is also required.[15] The outputs 1e, 2e, 2ch of this module are signals active respectively when one electron, two electrons, or two charged tracks are identified. The logic is done with LRS NIM modules in about 70 ns.

The multiplicity module provides the numbers NH2 and NSF of H2 scintillators and fiber bundles that respectively counted. It is built from LRS 4532 majority logic modules that give output signals proportional to the number of active input signals. The multiplicities selected from this module are: $NH2 = 2$, $NH2 \leqslant 4$, $NH2 = 3,4$ and $NSF = 3,4$, and the combined multiplicities $NH2 + NSF = 7,8$. It requires about 65 ns.

The coplanarity module requires at least two hits in H2, back to back within 22.5°. This module uses only the signals coming from the H2 hodoscope and requires that, if an element of H2 is hit, then at least one of the 3 opposite elements are hit. It requires about 50 ns.

The neutral-veto module provides a veto for the neutral trigger. The logic selects *charged tracks* based on coincidences between corresponding H1 and H2′ counters. The OR of all 8 *tracks* is taken as the veto. It requires about 40 ns.

To reject events with tracks at polar angles that are too small to be within the tracking system

[15] To improve the efficiency, the OR of the corresponding H2 elements is enlarged to the neighboring elements, requiring a 1 vs. 6 coincidence.

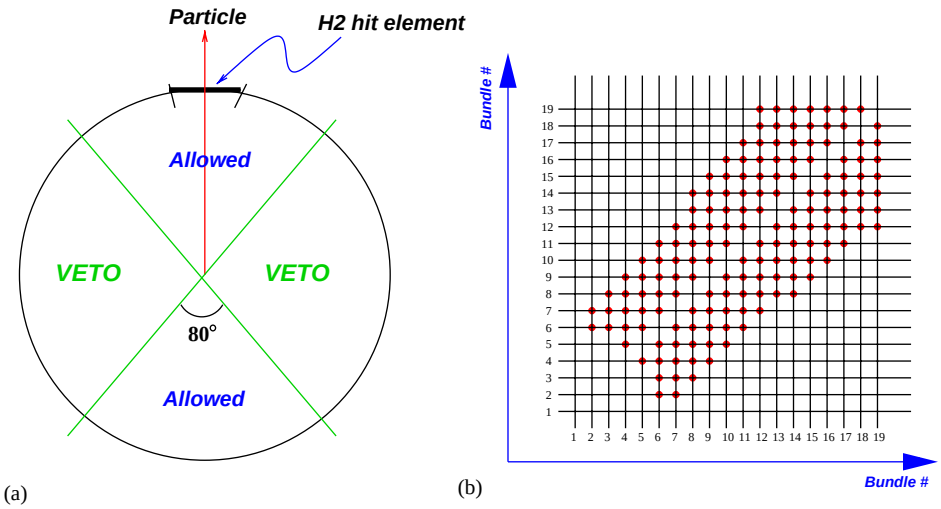

Fig. 36. Principles of the $\phi\phi$ trigger logic. (a) Back-to-back events are selected by requiring, for any H2 hit, that additional hits are limited to the allowed regions, each 7 counters wide (separated by two veto regions each 9 counters wide); (b) The coincidence matrix of scintillating-fiber bundles consistent with $\phi\phi$ kinematics.

acceptance, the forward veto, an OR of the signals from the forward charged hodoscope, is formed using the current sum output of a dedicated discriminator.

The $\phi\phi$ trigger requires highly selective and efficient logic. The first element (H2_$\phi\phi$) requires that, if an H2 counter is hit, two back-to-back azimuthal regions 80° wide are considered, centered about the hit scintillator and its opposite element. The event is accepted only if no hits are present outside the above regions (see Fig. 36a). The second element (KIN_$\phi\phi$) exploits the capabilities of the scintillating fiber detector. It consists of a matrix of coincidences between the fiber-bundle signals, designed ad hoc to select events that satisfy $\phi\phi$ kinematics (see Fig. 36b). Each one of the elements is implemented using a LRS 2366 Universal Logic Module. These are configured through an EPROM that contains the required pattern of logical operations. The transit time of the H2 logic is about 40 ns, while for the $\phi\phi$ kinematic logic the time varies from 33 to 36 ns. Since in the $\phi\phi$ reaction the kaon polar angles are always smaller than 60° we implement the $\text{VETO}_{\phi\phi}$ element using scintillating fiber bundle #1 (Fig. 37).

The output signals of the single-logic modules are sent to custom CAMAC programmable memory-lookup units (MLU). The C_MLU combines the logic elements for the selection of events with e^+e^- in the final state; the ϕ_MLU combines the logic elements for the $\phi\phi$ channel. The outputs of these units, joined by that from the N_MLU used for the neutral channel selection, are sent to the M_MLU. These modules are configured, via CAMAC, in such a way that each output can be any logical combination of the incoming signals. The output levels are determined at the trailing edge of a strobe signal in order to synchronize the output signals for different triggers. The output of the M_MLU is strobed into the DAQ system, which then writes the event.

The strobe signal for the C_MLU and the ϕ_MLU is the OR of the H2 hodoscope signals. Since the timing of this signal is critical, it is reshaped using an Ortec 934 constant fraction discriminator, which leads to a jitter of 2 ns or less. Input signals that arrive at least 8 ns before the strobe are successfully latched. To allow for a 5 ns jitter, the inputs are set to reach the MLUs 15 ns before the strobe and are 30 ns wide. The strobe itself must be at least 6 ns wide and we choose 10 ns.

The transit time through the single-logic stage of the charged trigger is 96 ns for the e^+e^- branch, and 106 ns for the $\phi\phi$ branch. From the final

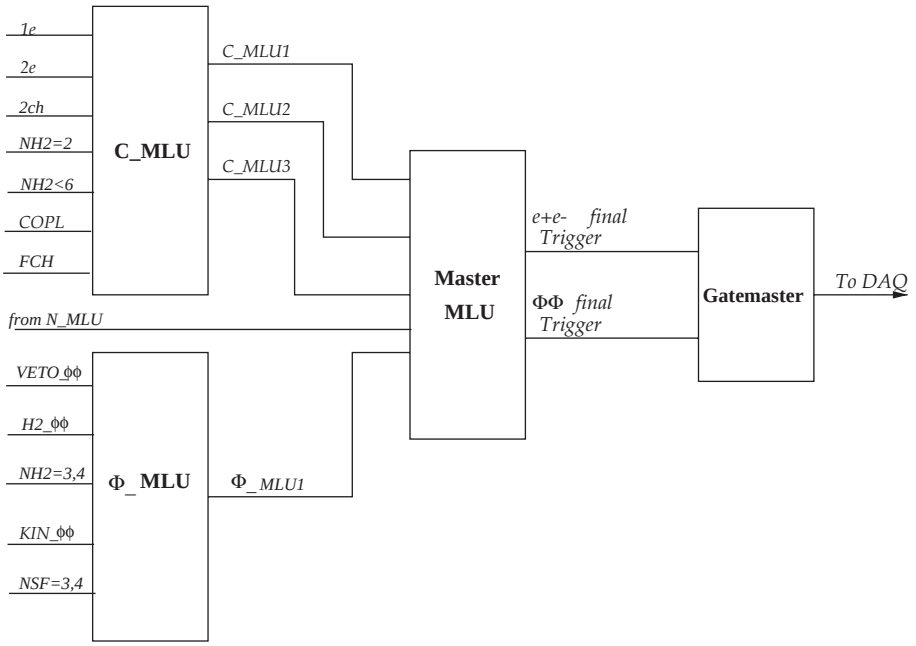

Fig. 37. The final charged trigger stage.

trigger stage to the output of the M_MLU it is about 90 ns (including some delay needed for synchronization with the neutral logic). The total transit time through the whole trigger is thus about 200 ns.

6.2. Charmonium neutral final states

The E835 neutral trigger is modified from the E760 neutral trigger [34]. It is constructed using signals from the CCAL alone and it is designed to trigger on two event types: charmonium electromagnetic final states, with two large invariant mass clusters from two photons or electrons from J/ψ or ψ' decays, and multi-photon final states, from $\bar{p}p$ annihilations into light mesons (π^0, η, ω) with all of the energy in the CCAL.

The trigger is based on event topology and the requirement for two large deposits of transverse electromagnetic energy. We first reduce the number of elements from 1280 to 160 signals consisting of the sum of 9 counters in the same ring (forming a super-wedge) overlapping with adjacent sums within the same ring. These super-wedge signals are then split with one path being discriminated at $\sim$100 MeV and the other path being summed in the ring direction to form 40 super-clusters. Super-rings and super-wedges are shown in Fig. 38. Each supercluster spans 9 wedges and 5 rings (with the exception of the superclusters constituting super-ring 1, which span rings 1–4) and overlap the adjacent superclusters (see Fig. 38). The overlaps prevent trigger inefficiencies for particles hitting the peripheral blocks of a super-cluster.

The logic is shown in Fig. 39. The 40 signals are discriminated and input to the N_MLU to produce two level-1 triggers (PBG1 and PBG3) for large invariant mass two-body events. Two additional triggers for multi-photon ($\pi^0\pi^0$, $\pi^0\eta$, etc.) events called ETOT-HI and ETOT-LO are formed. The ETOT signals are formed by summing the CCAL counters without overlaps. The strobe for the N_MLU is based upon having at least two of the super-wedge signals above the discriminator threshold.

- PBG1 requires that the inputs corresponding to two back-to-back super-wedges are both on, i.e. it requires consistency with two body

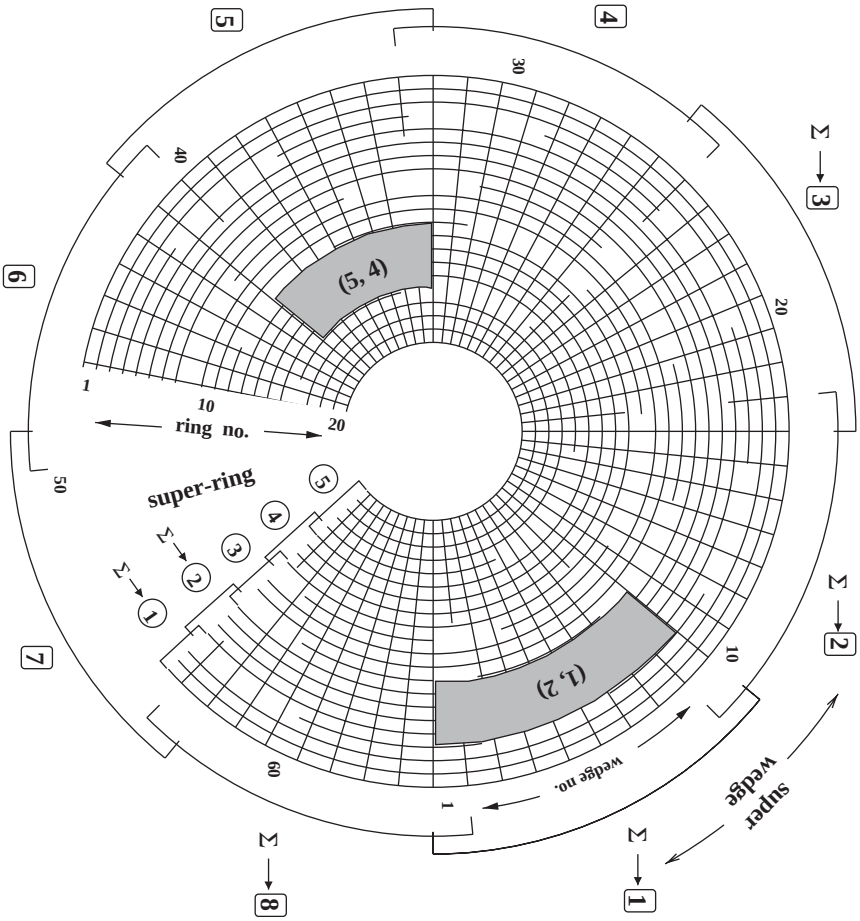

Fig. 38. Diagram of the 1280 CCAL blocks. Super-ring and super-wedge boundaries are indicated by the heavy solid and dashed lines. Superclusters $(SW, SR) = (1, 2)$ and (5,4) are also shown.

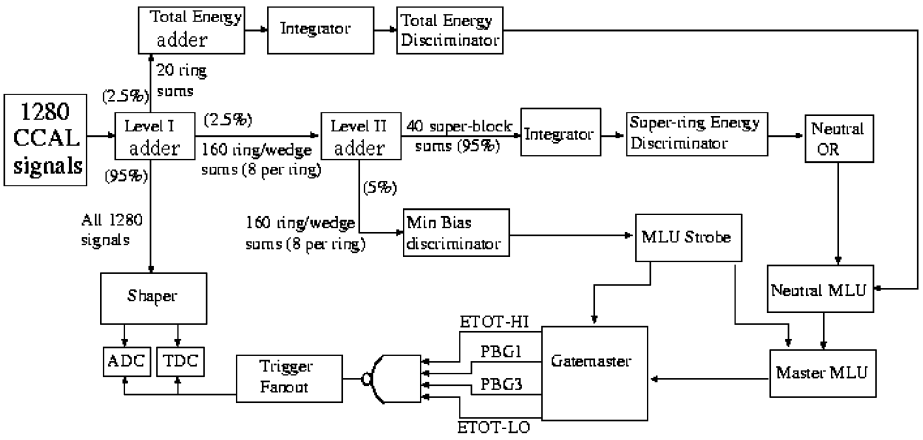

Fig. 39. Block diagram of the neutral trigger logic. The percentages in parentheses refer to division of the signal inputs.

Table 9
Efficiencies of the neutral trigger for charmonium (PBG1) and multiphoton (ETOT-HI) final states as a function of center of mass energy

Res.	$\sqrt{s}$ (GeV)	PBG1 eff. (%)	ETOT-HI eff. (%)
η_c	2.99	99.5	99.8
J/ψ	3.10	100	100.
Cont.	3.25	98.8	99.8
χ_0	3.41	100.	99.8
χ_1	3.51	100.	99.1
$^1P_1$	3.53	99.4	99.3
χ_2	3.55	99.7	99.0
η_c'	3.60	100.	98.2
ψ'	3.67	100.	97.7
Cont.	3.70	100.	95.0

kinematics. It is designed to trigger on $\gamma\gamma$ and exclusive e^+e^- events.
- PBG3 is similar to PBG1 but with a looser coplanarity requirement; it requires a coincidence between a super-wedge and one of three opposite super-wedges and is implemented mainly for $e^+e^-\gamma$ events, where the two electrons are not coplanar.
- ETOT-HI requires the total energy in the CCAL exceeds 80% of the available energy.
- ETOT-LO The same as ETOT-HI with the threshold at 70% of the available energy.

The formation time of the PBG triggers is 200 ns and that of the energy triggers is 155 ns. In Table 9 PBG1 and ETOT-HI efficiencies are summarized for various physics channels.

7. The data acquisition system

E835 acquires data from four independent data acquisition streams running in parallel: the event data stream, the beam parameter data stream, the luminosity monitor data stream and the scaler data stream.

The event data stream is based on DART [35], a system developed in collaboration between the Fermilab Online System Department and several experiments that operated during the 1996–97 fixed target run. DART provides a common system of hardware and software, which we have configured and extended to meet specific E835 requirements.

The beam parameter information data stream is received from the FNAL Beams Division via ethernet.

The luminosity monitor and scaler data streams are input via CAMAC.

Three Silicon Graphics (SGI) computers are used to coordinate, process, filter, log and monitor the data streams. The run-control computer (SGI INDY) coordinates the independent data streams, communicates with the CAMAC branches and performs the slow data acquisition functions. The event data acquisition, which consists of event building, filtering and logging, is performed by an SGI CHALLENGE-L with 4 processors in 1996/1997 and 12 in 2000. The monitor display computer, which monitors the detectors and displays events, is a SGI INDIGO.

7.1. Data streams

7.1.1. Event data acquisition stream

The event data acquisition hardware layout is shown in Fig. 40. The 1996/1997 readout electronics consists of 163 ADC (LRS4300), 66 TDC (LRS3377) and 23 PCOS modules (LRS2731), organized in 14 CAMAC crates. In 2000 the PCOS modules were replaced by additional TDCs. They are arranged in 3 CAMAC branches, two parallel and one serial, and addressed by the run-control computer through two SCSI 411 Jorway Interfaces.

Data from the detectors are read by the ADC, TDC and PCOS modules, and transferred through their front-end ECL-ports to the DART-developed DYC module. The DYC is an intermediate data buffer which stores the 16-bit input data in a 32-bit wide FIFO. It adds a header word including a word count, an error bit in the case of event overflow, and 4 bits of event synchronization. Data is sent to two Access Dynamics DC2/DM115 module pairs[16] over RS-485 cable. Each ADC or TDC CAMAC crate is served by a DYC. It responds to the request from the readout electronics modules it serves, which are connected

[16] Access Dynamics, Inc., 3823 Hawkins St. NE, Albuquerque, NM 87109, USA.

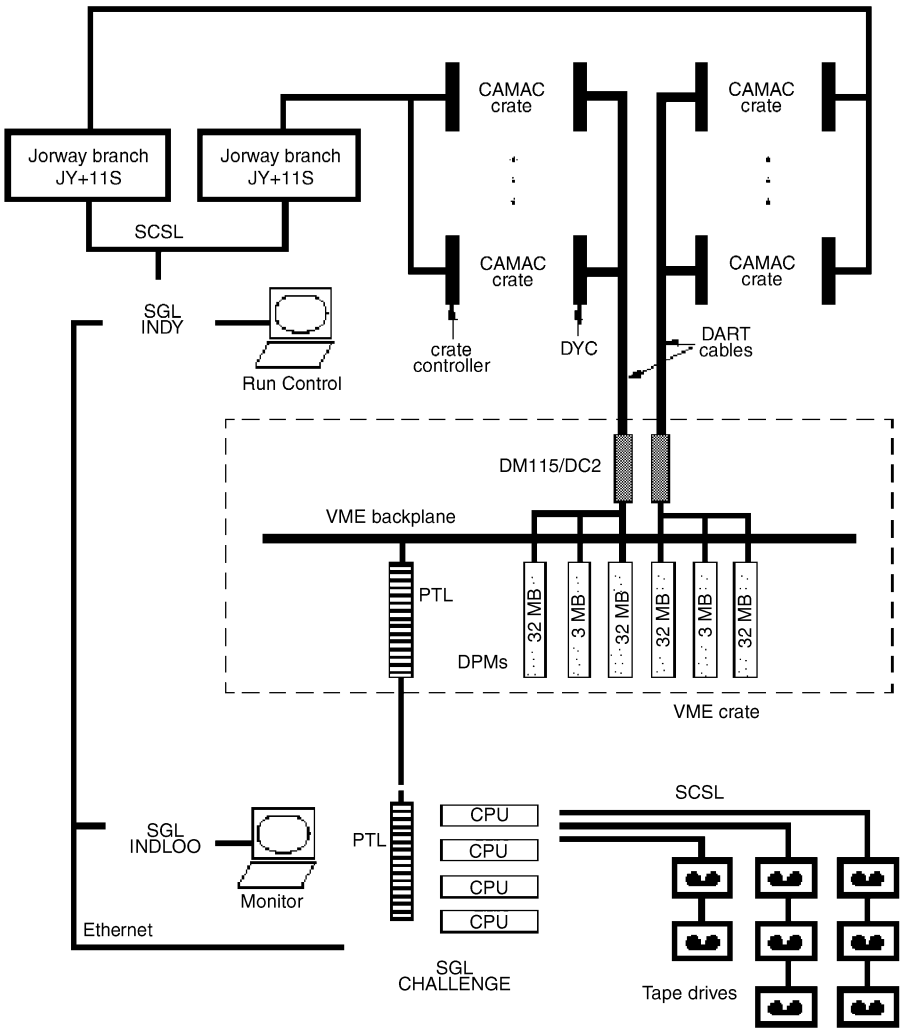

Fig. 40. E835 data acquisition hardware layout.

in a daisy-chain, by issuing a *readout enable* to the first module, starting the data transfer. When the first electronics module has finished sending data, it enables the following module by sending a *pass* signal. The end of the data transfer is signaled by receipt of the pass signal from the last module.

All of the PCOS modules, arranged in two CAMAC crates, are served by a single DYC, which communicates, via a Fermilab ECL Data Adapter (EDA-PD31),[17] with two PCOS controllers, one in each crate. The PCOS data are collected by these controllers via the CAMAC backplane and sent, via front-end ECL port, to the DYC via the EDA-PD31.

While receiving data, the DYC modules issue busy signals. The "OR" of these busy signals is sent to the trigger logic to inhibit triggers during data transfer. The DYCs are connected in a daisy-chain via two RS-485 cables (labeled as DART cables in Fig. 40) in two groups, each connected to one of the DC2/DM115 pairs. Data transmission to a DC2/DM115 is controlled by a wait signal established by the destination buffer, and a permit

[17] http://www-esd.fnal.gov/esd/catalog/main/fermilab/pd-31.htm.

token. On receipt of a permit token and in the absence of a wait signal, the DYC transmits the header word and data for one event. When it has completed its transmission, it passes the permit token to the next DYC. The DYC module is able to simultaneously perform the data reception from the readout electronics modules and the data transmission to the DC2/DM115.

Each DC2 is connected, via the VSBus of the VME crate, to two 32 MB and one 8 MB Dual Ported Memories (DPM) MM-6390.[18] Each DC2 fills its two 32 MB DPMs with the data it receives from the DYCs using a *ping-pong* algorithm, in which it writes the *ping* DPM with exactly N (set in the configuration database) events before it switches to the *pong* DPM.

The *gateway* process, running on the Challenge, reads data from the *ping* DPM via PTI (PT-VME64)[19] while the DC2 writes data to the *pong* DPM. When all the data from the *ping* DPM are read, gateway allows the DC2 to write to the *ping* DPM while it reads data from the *pong* DBM. Both the DC2 and gateway poll to determine if the other has finished using a DPM. They communicate using the 8-MB DPM as a mailbox. Neither the DC2 nor gateway interrupt a data transfer while polling.

Gateway writes the two DC2 data sets, which comprise N events, to one of two *gateway buffers* in a reserved part of the Challenge-L's memory, designated as memory to be shared among processes. After writing to a gateway buffer, gateway releases it to a filter queue before writing to the other buffer in shared memory. A filter process is continuously running on each CPU of the Challenge-L. Each filter queues for a gateway buffer. When one is available, it *builds* the N events it contains, using data from both DC2 data sets and adding an event header, which includes a unique event number, the date and time of processing, and pointers to DYC header words for offline use. Several *trigger-classification* and *online-analysis* flags are included. Synchronization numbers of the DPMs and the DYCs are checked and the data integrity is verified for 0.1% of the events processed. The trigger information is decoded to classify the event in order to determine which online analyses to perform, if any, and to which logging stream the event, if not rejected, is sent.

We perform the following online analyses:

- a simplified CCAL determination of energies and angles for electromagnetic showers and formation of invariant mass pairs, to identify π^0, η and $\bar{c}c$ candidates,
- simple charged-track reconstruction with electron identification and association with CCAL energy deposits, for identifying $\bar{p}p \to e^+e^-$ and $\bar{p}p \to J/\psi + X \to e^+e^- + X$,
- and/or identification of events with four charged tracks which loosely satisfy the kinematics of $\bar{p}p \to \phi\phi \to 4K^{\pm}$.

The filters set analysis bit flags in the event header word and write summary event information, which is added to the end of the event. The analysis bit flags are compared to a list of trigger masks to determine acceptance of the event.

Accepted events are copied to logging buffers reserved in the shared memory for recording to tape and transfer to the monitor-display computer. There are three logging streams; the trigger-classification and online-analysis flags determine which stream an event is written to. Events for which the filter determines a large invariant mass and those to be used for calibration are copied to other logging buffers. When the logging buffers are full (maximum size 64 KBytes and average event size $\sim$1 KBytes), they are released to appropriate logging queues or to the monitor-display computer. There are 5 logging processes, each with its own queue and tape drive. Each process receives buffers from all of the filter processes.

7.1.2. Beam parameter data stream

The control and monitoring of the FNAL accelerator complex is performed through the ACNET[20] (Accelerator Control NETwork) system. Accelerator data for E835 is acquired by a

[18] Micro Memory, Inc., 9540 Vassar Ave., Chatsworth, CA 91311, USA.

[19] Performance Technologies—http://www.pt.com.

[20] http://www-bd.fnal.gov/controls/acnet.html

FNAL Beams Division ACNET computer, which is interfaced to the accelerator instrumentation and sends a data stream to the run-control computer, consisting of positions and intensities recorded by beam position monitors, the longitudinal frequency spectrum of the beam, the gas-jet density, pressures within the accelerator, magnet currents, magnetic field strengths, and the online determination of the beam energy, emittances and current. The run-control computer writes the accelerator data to disk, depending upon the status of the run control. The online beam momentum and beam current are unpacked and made available for monitoring purposes.

7.1.3. Luminosity monitor data stream

The (CAMAC) readout electronics of the luminosity monitor detector consists of a multiplexed ADC converter (EGG ORTEC[21]-AD413A) and a FERAbus Histogramming Memory (EGG ORTEC-HM413).

A self-gating ADC channel is used to read each of the three silicon detectors. Each channel is read and histogrammed via the front-end ECL port by the HM413 module.

Every two minutes a process running on the run-control computer reads the three data sets from the HM413 module via the CAMAC backplane, resets the memory, computes the luminosity, writes the result on disk, and sends it to the monitor-display computer.

7.1.4. Scaler data stream

The readouts of the scaler data stream and luminosity monitor share a CAMAC crate. Three LRS4434 scaler modules receive data—via their front-end ECL ports—from the trigger and detector electronics. A FNAL CAMAC pulser (RFD01) module[22] sends a signal to the scalers to update every 10 seconds. The data stream is sent via the CAMAC backplane to the run-control computer which writes it to disk and displays it on a monitor.

[21] EGG ORTEC, 100 Midland Rd., Oak Ridge, TN 37830, USA.

[22] http://www-esd.fnal.gov/esd/catalog/main/fermilab/rfd01.htm.

8. The offline event reconstruction

8.1. Tracking

Tracking of charged particles by the inner detectors is done separately for the $r-\phi$ and $r-z$ projections. The straw chambers are used for $r-\phi$ and the scintillating fibers together with the nominal position of the interaction vertex for $r-z$. The projections are associated using CCAL information.

8.1.1. Reconstruction of the track ϕ angle

We determine ϕ for charged tracks using the straw chambers. We first determine the drift distance within the hit straw and then fit a straight line through the layers using the geometrical parameters of the straws.

For each straw the discriminator threshold is set at one primary ionization. To a good approximation the first arriving hit is detected.

We define the *drift time*, which is measured with 500 ps (rms) resolution,[23] as the delay of the straw signal with respect to the event time, the latter defined by a strobe constructed from CCAL signals. The drift-time distribution of a single straw is shown in Fig. 41. Particles crossing the straw close to the wire (*early times*) correspond to the right side of the plot. For each straw we measure a reference time T_0, which depends on the propagation delays through the electronics and cables. The T_0 are determined from plots such as Fig. 41 by fitting the *early times* part of the distribution to a straight line.

The drift-time distributions $(T-T_0)$ for all straws in each layer are shown in Fig. 42. For constant drift velocity and full efficiency, we would have uniform drift-time distributions since the particle density is uniform in ϕ. We correct for non-constant drift velocity and obtain $X(T-T_0)$ for each layer using:

$$\frac{X(T-T_0)}{R}=\frac{\mathrm{d}N}{\mathrm{d}X}\int_{T_0}^{T_1}\frac{\mathrm{d}X}{\mathrm{d}t}\frac{\mathrm{d}t}{N}$$

where N is the total number of tracks, $\mathrm{d}N/\mathrm{d}X$ $(=\text{constant})$ is the track density, and X is the

[23] LRS multihit TDC 3377 used in Common Stop mode.

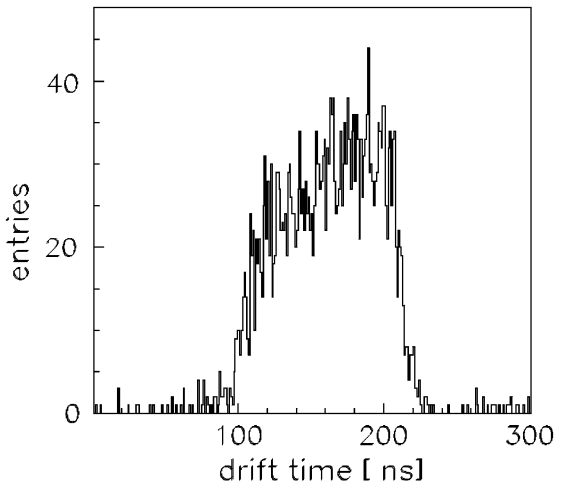

Fig. 41. The drift-time distribution of a single straw in the outer chamber.

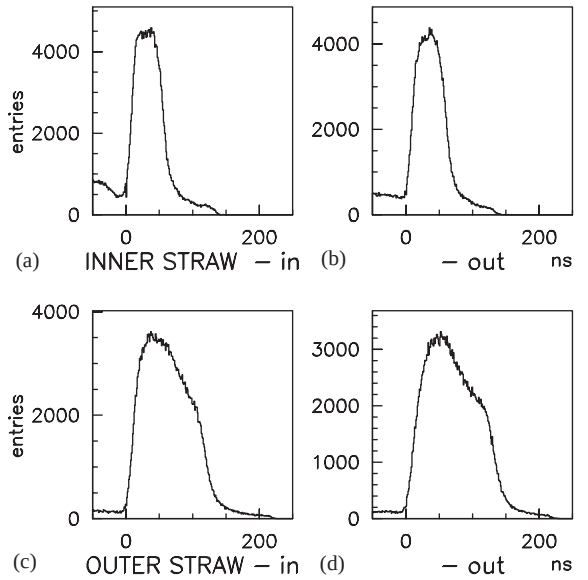

Fig. 42. Drift-time distributions for the four layers of straw chambers.

perpendicular distance between the particle line of flight and the wire, which determines ϕ and is independent of θ.

For each track we fit a straight line through the hits to determine ϕ. In Fig. 43, we show the distribution of the deviation from π of the difference between ϕ for the e^+ and e^- tracks in a sample of $\bar{p}p \to J/\psi$. The width implies a single-track rms resolution of $\simeq 9$ mrad.

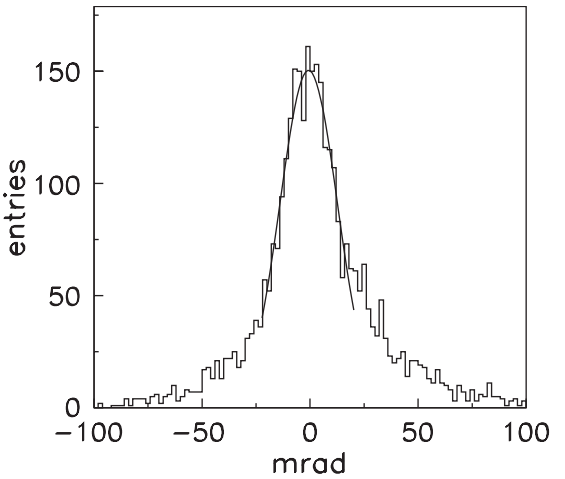

Fig. 43. Distribution of the deviation from π of the difference between ϕ for the e^+ and e^- tracks in a sample of $\bar{p}p \to J/\psi$.

8.1.2. Reconstruction of the track polar angle

We determine θ for charged tracks using the scintillating fiber detector.

A charged particle traversing the scintillating fiber detector hits up to three consecutive fibers in each layer, depending on θ. Clusters are sets of adjacent hit fibers; those with more than three fibers are split into two or more smaller clusters. The z coordinate of the intersection between the track and the layer is taken as the weighted (by the energy deposit in each fiber) mean of the z coordinates of the fibers in a cluster. It is converted into a θ coordinate using the nominal coordinates of the interaction point.

Then the clusters found in each layer are associated to form tracks, by requiring that their θ angles be within a specified range. The clusters for each track and the interaction point determined using the CCAL, described in Section 8.3, are fit to a straight line.

8.2. Calorimetry

A calorimeter *cluster* is a 3×3 set of active CCAL counters associated with a charged particle or photon. The clusterizer groups active blocks

into clusters and assigns a position and energy to each.

A cluster *seed* is a block with more energy than the eight surrounding blocks. It is required to have a minimum energy, the *seed threshold*, which depends upon the analysis being performed. The summed energy of the cluster seed and the eight surrounding blocks is also required to have a minimum energy, the *cluster threshold*, which also depends upon the physics analysis.

If two clusters overlap, the energy in the common blocks is shared, the jth cluster taking a fraction f_i^j of the energy E_i in the ith block. Cluster positions, energies, and f_i^j are calculated iteratively as described below.

The cluster position is first approximated as the energy-weighted average of block coordinates. Defining (x^j, y^j) as cluster coordinates in units of blocks, in the (θ(wedge),ϕ(ring)) directions, where the origin is the center of the seed block, we have

$$x^j = \frac{\sum_{i=1}^{9} f_i^j E_i x_i}{\sum_{i=1}^{9} f_i^j E_i}, \quad y^j = \frac{\sum_{i=1}^{9} f_i^j E_i y_i}{\sum_{i=1}^{9} f_i^j E_i} \tag{21}$$

where $x_i = -1, 0, 1$ and $y_i = -1, 0, 1$ are the coordinates of the centers of blocks in the cluster in block units.

The steel partitions between the blocks represent 2% of the surface area of the CCAL in the ϕ direction and 0.5% in the θ direction. Energy from the showers is lost in these *cracks* and corrections to both the position and energy of the shower are made. The correction to the cluster position is based upon the shower profile and is computed as follows:

$$\begin{aligned} x' &= N_x[A_w a_w(1 - \mathrm{e}^{-x/a_w}) + B_w b_w(1 - \mathrm{e}^{-x/b_w})] \\ N_x &= 0.5/[A_w a_w(1 - \mathrm{e}^{-0.5/a_w}) + B_w b_w(1 - \mathrm{e}^{-0.5/b_w})] \\ y' &= N_y[A_r a_r(1 - \mathrm{e}^{-y/a_r}) + B_r b_r(1 - \mathrm{e}^{-y/b_r})] \\ N_y &= 0.5/[A_r a_r(1 - \mathrm{e}^{-0.5/a_r}) + B_r b_r(1 - \mathrm{e}^{0.5/b_r})] \end{aligned} \tag{22}$$

where x' (y') is the distance in the wedge (ring) direction, in block units, from the center of the seed block. The constants A_w, A_r, a_w, a_r, b_w and b_r were measured empirically with e^+e^- decays of the J/ψ and are listed in Table 10.

Table 10
Constants used in calculating the position and energy of CCAL showers

A_r	724.4	a_r	0.03208
A_w	706.5	a_w	0.03969
B_r	123.6	b_r	0.1860
B_w	102.6	b_w	0.1715
C_l	0.0614	c_l	7.367
C_h	0.0857	c_h	19.690
D_1	0.14736	d_1	48.908
D_2	0.15935	d_2	12.761

The corrected energy is given by

$$E_\mathrm{corr} = \frac{E_\mathrm{meas}}{(1 - C_{\mathrm{h}(l)}\mathrm{e}^{-|x^*|/c_{\mathrm{h}(l)}})} \times \frac{1}{(1 - D_1\mathrm{e}^{-|y^*|/d_1} - D_2\mathrm{e}^{-|y^*|/d_2})} \tag{23}$$

where x^*, y^* are the distances from the cluster center to the closest edges of the seed block and the constants are listed in Table 10. The ring faces are staggered, (see Fig. 20) and $c_\mathrm{h}(c_\mathrm{l})$ corresponds to the high(low) θ block edge. The effectiveness of this algorithm is demonstrated by Fig. 44.

At the largest $\sqrt{s}$, the smallest π^0 opening angle corresponds to approximately 1.5 block widths. If the two photons hit blocks whose corners touch diagonally, only one of the blocks would be considered a cluster center by the clusterizer, and one cluster would be found instead of two. These coalesced π^0s that are not separated by the clusterizer must be identified and split into separate clusters. We calculate the *cluster mass*, M_cl, for every cluster, where we sum over 25 blocks in a 5×5 grid around the seed.

$$M_\mathrm{cl} \equiv \sqrt{\left(\sum_i E_i\right)^2 - \left(\sum_i \vec{p}_i\right)^2} \tag{24}$$

E_i is the energy deposited in the ith block of the cluster and $\vec{p}_i \equiv E_i \hat{r}_i$ where $\hat{r}_i$ is the unit vector from the interaction point to the center of the ith block. Fig. 45 shows the cluster mass for e^+e^- pairs from J/ψ decay and for clusters formed in π^0 decays. The large peak at the π^0 mass represents the coalesced π^0s, and the small peak the isolated photons from asymmetric π^0 decays. Any cluster with $M_\mathrm{cl} > 100$ MeV is split into two by choosing a

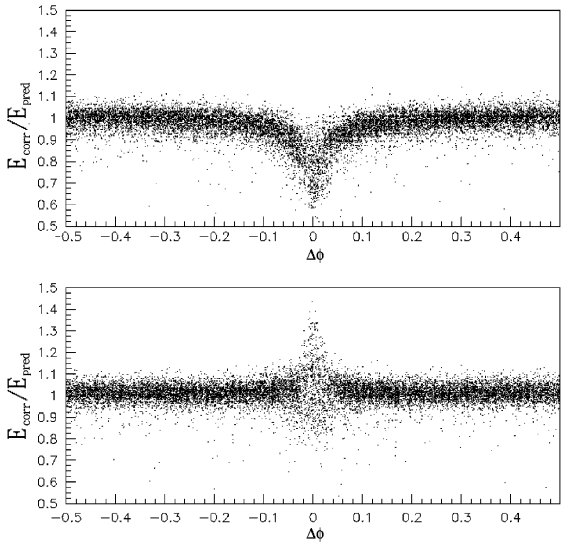

Fig. 44. Crack correction in the CCAL. The upper plot is the ratio of predicted to measured energies one for good π^0 events, as a function of the distance from the nearest crack. The lower plot is the same after crack correction.

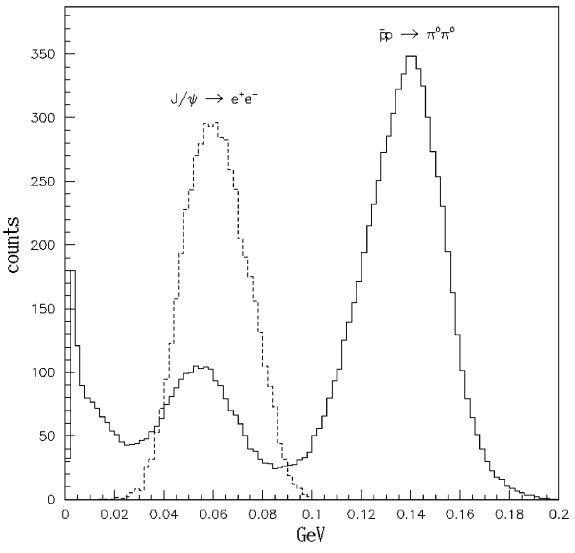

Fig. 45. Distribution of $M_{\rm cl}$ for $\pi^0\pi^0$ events (solid) and e^+e^- decays of the J/ψ (dashed). A cluster is split if its $M_{\rm cl}$ is greater than 0.1 GeV.

second cluster center as the block with maximum energy among the four corner blocks of the 3×3 grid centered at the original cluster center. The energy of each cluster is then determined using the

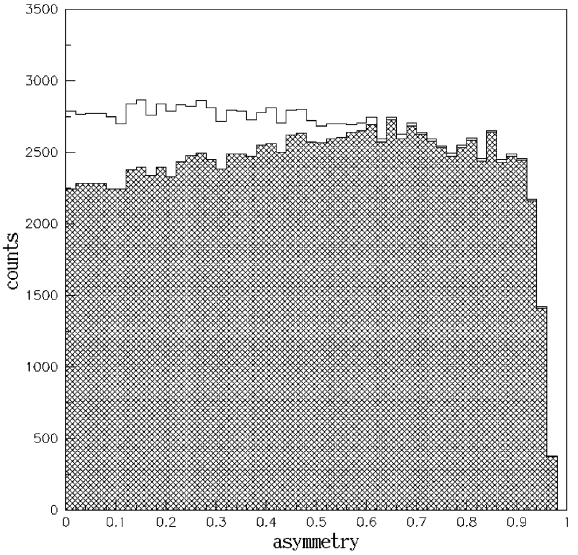

Fig. 46. Distribution of the π^0 asymmetry $(E_1-E_2)/(E_1+E_2)$ plotted without the split clusters (shaded) and including the split clusters (open). The distributions are expected to be uniform.

sharing algorithm described above. Fig. 46 demonstrates the π^0 recovery power of the cluster-splitting method.

8.3. CCAL calibration

We calibrate the CCAL both with e^+e^- events from J/ψ and ψ' decays and with $\pi^0\pi^0$ events. The calibration with $\pi^0\pi^0$ events is superior because many more events are available (from ≈ 7500 events per pb^{-1} at the ψ' energy to $\approx 150,000$ events per pb^{-1} below the η_c energy), because events are collected at each energy point, so each stack can be independently calibrated, and because γs from these events populate every counter of the detector.

A clean $\pi^0\pi^0$ sample is selected for each stack using the following procedure: among the possible combinations of two of the four photons to form a π^0, that with the smallest value of $\sqrt{(2\Delta\theta)^2+(\Delta\phi)^2}$ is chosen, where $\Delta\phi \equiv \pi - |\phi_1 - \phi_2|$ and $\Delta\theta \equiv \theta_{1\rm pred} - \theta_{1\rm meas}$, where $\theta_{1\rm meas} \leqslant \theta_{2\rm meas}$ and $\theta_{1\rm pred}$ is obtained from $\theta_{2\rm meas}$ by kinematics. θ

Table 11
Criteria for $\pi^0\pi^0$ event selection

	Energy calibration	Vertex determination	Timing calibration
Seed/cluster threshold	25/50	25/50	5/20
Ring restriction	None	None	None
$\lvert\Delta\theta\rvert$ (mrad)	<10	<10	<15
$\lvert\Delta\phi\rvert$ (mrad)	<32	<32	<30
$\lvert M_\pi - 135\rvert$ (MeV)	<40	<35	<35
CCAL clusters	Exactly 4	Exactly 4	Exactly 4
	Neutral DST efficiency	Monte Carlo testing	$\pi^0\pi^0$ cross-section
Seed/cluster threshold	25/50	5/20	25/50
Fiducial volume	Rings 2–18	Rings 2–18	Rings 2–18
$\lvert\Delta\theta\rvert$ (mrad)	15	15	2σ
$\lvert\Delta\phi\rvert$ (mrad)	32	30	30
$\lvert M_{\gamma\gamma} - 135\rvert$ (MeV)	35	35	35
CCAL clusters	4 i.o.u.	Exactly 4	4 i.o.u.

"i.o.u." stands for "in-time or undetermined" clusters, as described in the text.

and ϕ are laboratory-frame angles. Depending upon the calibration procedure, the sample is subjected to different criteria, summarized in Table 11 with the distributions shown in Fig. 47, and based on the following:

- Energy and seed thresholds used in the clusterizer; see Section 8.2 for the description of the thresholds.
- Fiducial volume where all four photons are within a specified set of CCAL rings.
- Maximum $\Delta\phi$(*acoplanarity*) accepted for both π^0.
- Maximum $\Delta\theta$(*akinematics*) accepted for both π^0.
- Acceptable range of *invariant mass* $\equiv M_\pi = (2E_{\gamma_1}E_{\gamma_2}(1-\cos\Theta_{\text{open}}))^{1/2}$, where Θ_{open} is the angle between the two photons in the laboratory frame. This criterion is not applied to π^0 derived from a split cluster.
- Number of CCAL clusters in the event. See Fig. 47d for the number of out-of-time clusters distribution; the timing description is given below.

Since the event selection depends (weakly) on the energy calibration, it is repeated after the energy-calibration procedure described below, followed by recalculation of the latter (Figs. 48 and 49).

8.3.1. Energy calibration

The CCAL *gain constant* g_i is defined as the ratio of energy deposited by a photon or electron in the ith block to the ADC value. These are determined using the full $\pi^0\pi^0$ sample for each stack by iterative χ^2 minimization.

The predicted energy of each π^0, E_j, is calculated from its polar angle using two-body kinematics. The energies contained in the n counters associated with the jth π^0 are summed to obtain the measured energy, M_j,

$$M_j = \sum_{i=1}^{n} g_i A_{ij} \tag{25}$$

where A_{ij} is the ADC value for the ith block. We construct χ^2 as

$$\chi^2 \equiv \sum_{j=1}^{N} \frac{(M_j - E_j)^2}{\sigma_j^2} \tag{26}$$

where σ_j is the estimated rms uncertainty in E_j, and N is the number of π^0s. The g_k that minimize χ^2 are given by

$$g_k = \frac{\sum_{j=1}^{N}\left(\frac{A_{kj}}{\sigma_j^2}\right)\left[E_j - \sum_{i=1,i\neq k}^{n} A_{ij}g_i\right]}{\sum_{j=1}^{N}\frac{A_{kj}^2}{\sigma_j^2}}. \tag{27}$$

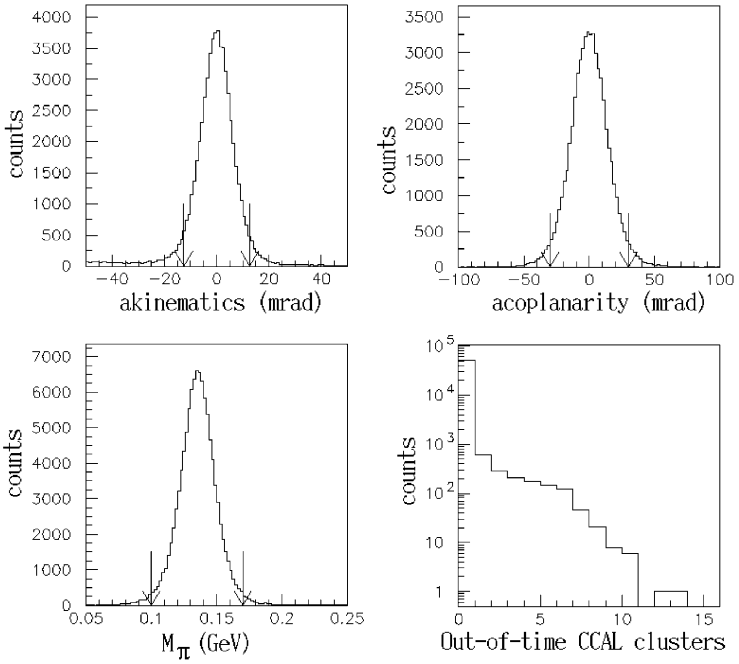

Fig. 47. Variables used to select clean $\pi^0\pi^0$ events. The arrows indicate the cuts used. The lower right plot shows the number of additional, out-of-time CCAL clusters per event after the selection cuts are made. The data are taken at $\sqrt{s} = 2990$ MeV and $\mathscr{L} = 0.76 \times 10^{31}$ cm^{-2} s^{-1}.

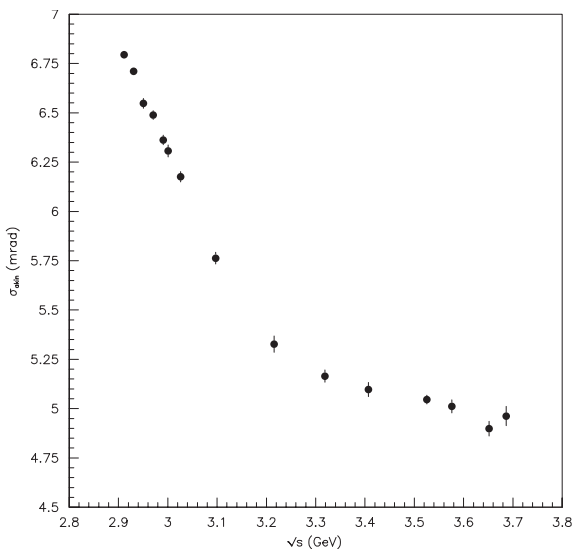

Fig. 48. The sigma of the akinematics distribution as a function of $\sqrt{s}$.

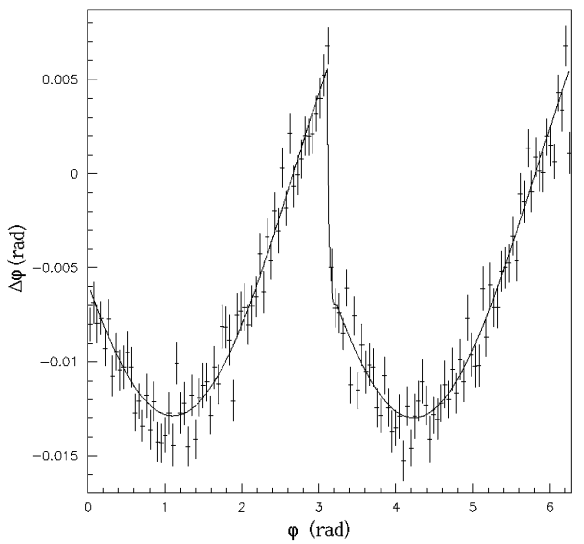

Fig. 49. The acoplanarity ($\Delta\phi$) distribution in ϕ for $\pi^0\pi^0$ data from stack 30.1, $\sqrt{s} = 3009$ MeV. The function drawn is Eq. (31) with $(x_0, y_0) = (-0.39, 0.2)$ cm.

These g_k are used in Eq. (25), and the procedure iterated until they converge. Gain constants are generally calculated for each stack. If for any (short) stack, the number of π^0 contributing to the calibration of the kth counter is less than 15, we retain the g_k associated with the previous stack.

8.3.2. Timing calibration

The multi-hit TDCs are used in *common stop* mode with a LSB of 1 ns, thus recording the time between the pulse leading edge and a pulse arriving approximately 10 ns after the end of the FERA gate. The entire window is 255 ns, sensitive to pulses arriving during the FERA gate or in the preceding 145 ns.

The CCAL counter timing parameters are obtained from the $\pi^0\pi^0$ sample. A representative turn-on curve, corresponding to a 5 mV discriminator threshold, is shown in Fig. 50. The fraction of ADC signals with a corresponding TDC signal is plotted as a function of ADC counts,

$$f = 0.5 \times (\mathrm{erf}(\mathrm{slope} \times (\mathrm{ADC} - \mathrm{thresh})) + 1.0) \quad (28)$$

where *slope* and *thresh* are parameters and f is the fraction of hits per ADC bin that have TDC information. The turn-on curve for every channel is measured periodically. Fig. 51 shows the distribution of turn-on parameters for the data taken in January 1997.

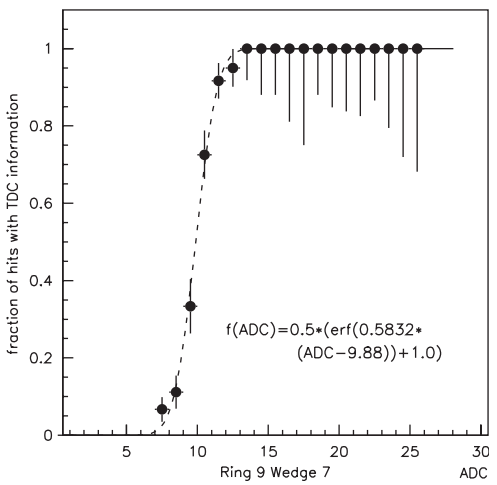

Fig. 50. A sample turn-on curve for a CCAL counter. The curve is a fit to Eq. (28).

These data are used to obtain slewing parameters for each counter. A plot of TDC vs. ADC values for a single counter is shown in Fig. 52. Events are included if there is exactly one TDC hit in the window $[T_0 - 40, T_0 + 60]$, which roughly corresponds to the FERA gate. T_0 is defined as the mean TDC value for pulses with A_0 ADC counts, where A_0 is the *thresh* parameter for the turn-on curve. The spread of T_0 values results from differences in cable lengths and PMT response times. The data are fit to

$$\mathrm{TDC} = T_0 + B_0 \times \left(1 - \frac{A_0}{\mathrm{ADC}}\right) \times \log(\mathrm{ADC} + E_0) \quad (29)$$

where B_0 and E_0 are parameters.

We have the following algorithm for CCAL timing:

- If there is more than one TDC hit in a counter, and at least one hit is in the window $[T_0 - 40, T_0 + 60]$ ns, the earliest hit within the window is chosen.
- If there are no hits within the window, the earliest hit is chosen.
- The counter is assigned a time using:

$$\mathrm{time} = 1000 + \mathrm{TDC} - [T_0 + B_0 \times \left(1 - \frac{A_0}{\mathrm{ADC}}\right) \times \log(\mathrm{ADC} + E_0)] \quad \text{for ADC} > A_0$$

$$\mathrm{time} = 1000 + \mathrm{TDC} - T_0 \quad \text{for ADC} \leqslant A_0 \quad (30)$$

where the offset 1000 is a convention.

In order to assign unique timing to a CCAL cluster, we consider the two counters with the most ADC counts. If neither has TDC information, the cluster is labeled *undetermined*. If either has a time within 10 ns of 1000, the cluster is labeled *in-time*. Otherwise, it is labeled *out-of-time*.

We study the efficiency and resolution of the cluster-timing algorithm using a separate set of $\pi^0\pi^0$ events that excludes split clusters. For cluster energies above 50 MeV, over 99.5% of the clusters are identified as in-time. Fig. 53 shows the fraction

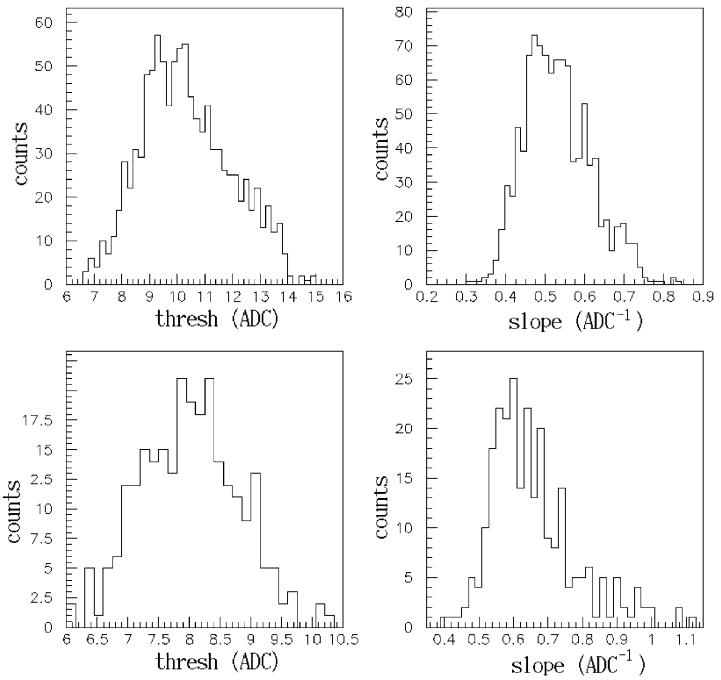

Fig. 51. Distribution of the turn-on curve parameters for every channel. Data from rings 1–16 are in the top two plots, with the threshold on the left and the slope on the right, and data from rings 17–20 are in the bottom plots.

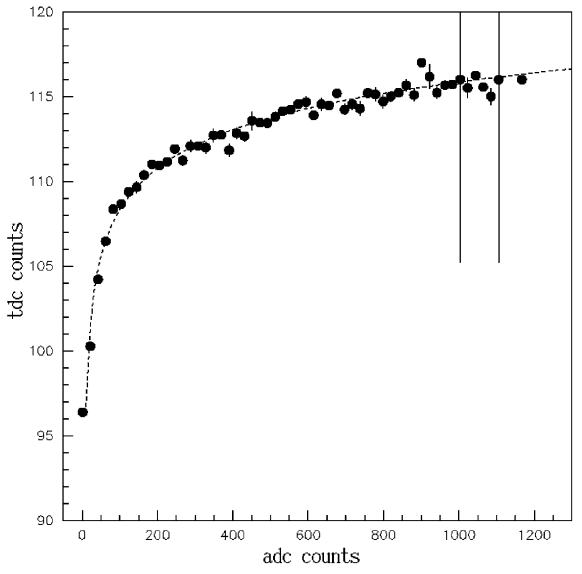

Fig. 52. An example of the ADC dependence of the TDC signal for a single counter, ring 9 wedge 7. The error bars represent rms uncertainties in the binomial probability f. The curve is a fit to Eq. (29) with $B_0 = 2.84$ and $E_0 = 3.59$.

of clusters with timing information as a function of cluster energy. When all of the pulses associated with a cluster are below discriminator threshold, a pulse from a prior interaction will cause it to be mistakenly identified as out-of-time. Thus, the frequency of out-of-time clusters increases with instantaneous luminosity. In Fig. 54, we show data taken at $\sqrt{s} = 2990$ MeV and instantaneous luminosities $\mathscr{L} = 0.76(2.02) \times 10^{31}$ cm^{-2} s^{-1}.

8.3.3. CCAL vertex determination

We require a nominal interaction point for the CCAL analysis in order to compute the laboratory angles of the clusters, thence the momentum of each photon. The interaction region is the intersection of the beam and the gas jet. While the jet location does not change, the beam position and size varies from stack to stack. For every stack, the (x, y) coordinate of the center of the interaction region is determined from the $\pi^0\pi^0$ sample. We obtain the desired precision of 0.1 mm using 10,000 events per stack.

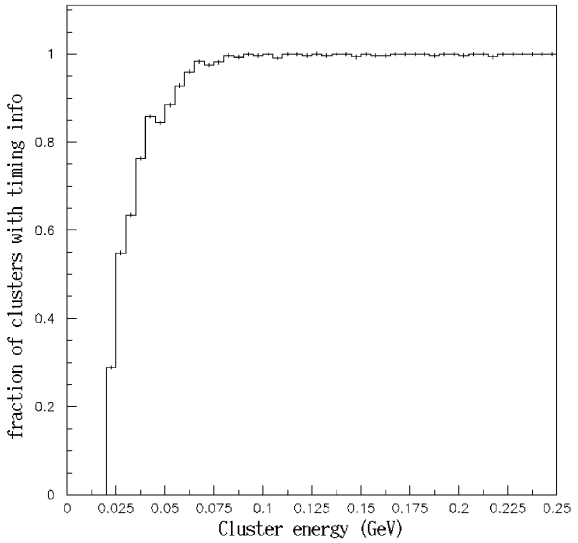

Fig. 53. The fraction of clusters with timing information as a function of cluster energy.

We define the laboratory coordinate system as follows: The z axis is the beam direction, the z coordinate of the gas-jet center is zero, the intersection point of the (pointing) counter axes of the CCAL is $(x, y) = (0, 0, z_c)$, the x–z plane passes through the axes of all of the counters of wedge no. 1 (see Fig. 38) of the CCAL.

For a two-body reaction, trigonometry gives the following formula for the *acoplanarity*, $\Delta\phi \equiv \pi - |\phi_1 - \phi_2|$, for a vertex at $(x_0, y_0, 0)$ where ϕ is the azimuthal angle of one of the π^0s and R is the counter radius in the x–y plane.

$$\tan\left(\frac{\Delta\phi}{2}\right) = \frac{x_0 \sin\phi - y_0 \cos\phi}{R - x_0 \cos\phi - y_0 \sin\phi}. \tag{31}$$

We fit the distribution of $\Delta\phi$ for each stack to Eq. (31) to obtain x_0 and y_0. As these parameters depend only on π^0 directions, (x_0, y_0) is relatively insensitive to the energy calibration, and we determine it, using the g_i from the previous stack, prior to the energy calibration, which depends strongly on (x_0, y_0). Fig. 55 shows the vertex positions for all the 1997 stacks.

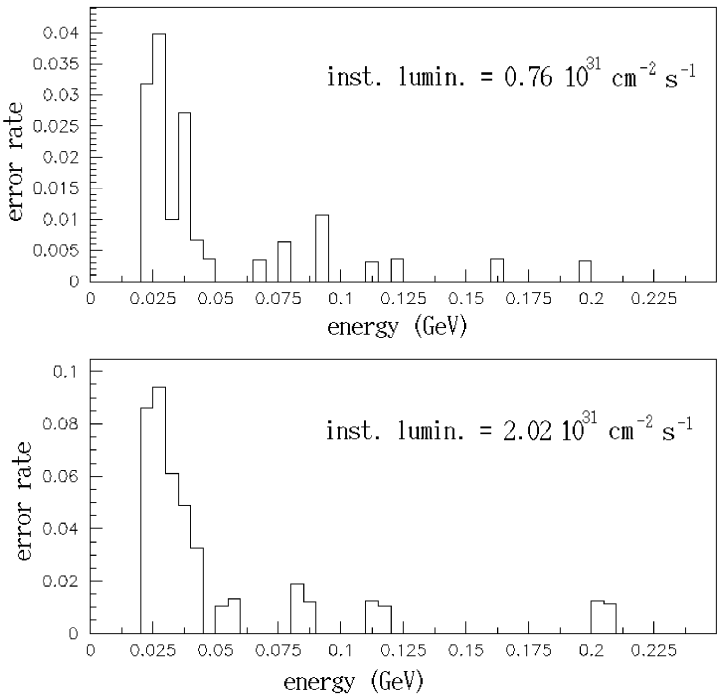

Fig. 54. The fraction of $\pi^0\pi^0$ clusters mistakenly identified as out-of-time as a function of cluster energy, for two different instantaneous luminosities. In both cases $\sqrt{s} = 2990$ MeV.

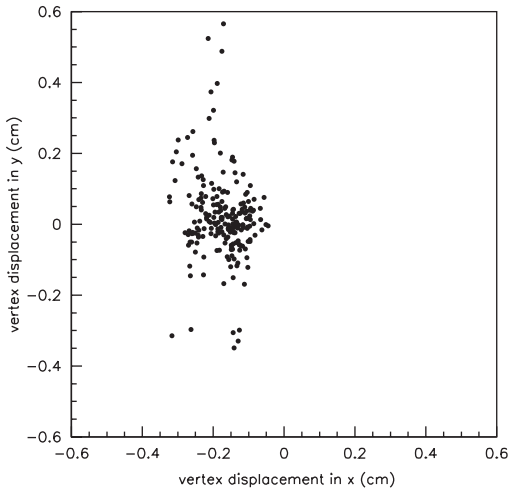

Fig. 55. Scatter plot of the x and y coordinate of the interaction vertex position reconstructed for all 1997 runs.

8.4. Electron identification

The experiment is designed to identify the electromagnetic decays of charmonium in a hadronic background which is between 10^8 and 10^{11} times larger. We require excellent electron identification and γ–π^0 separation. Individual electrons must be distinguished from other "tracks" producing Cherenkov light, including e^+e^- pairs due to photon conversion in the beam pipe and from Dalitz decays of π^0s.

The detectors that provide useful electron-identification information are the H1, H2 and H2′ scintillator hodoscopes, which measure dE/dx; the scintillating fiber detector, which measures dE/dx and can identify small-angle electron pairs; the threshold Cherenkov counter, which counts only electrons and can identify electron pairs using pulse height; and the CCAL, where cluster shapes are different for single electrons, hadrons and electron pairs.

We develop a likelihood ratio, which we refer to as the electron weight (EW), to combine the information from these detectors. A second method, the k-nearest neighbor rule [36], is used to check the assumptions of the EW method.

For each charged track, characterized by measured quantities $\mathbf{x} = (x_1, \ldots, x_n)$, we seek to distinguish between hypothesis e that it is an electron vs. hypothesis b that it is not an electron. The optimal (Neyman–Pearson) method is construction of the likelihood ratio $\rho(\mathbf{x})$, derived from the probability density functions (pdf) $F_e(\mathbf{x})$ and $F_b(\mathbf{x})$, under the two hypotheses respectively. For a single track we have

$$\rho(\mathbf{x}) = \frac{F_e(\mathbf{x})}{F_b(\mathbf{x})}. \tag{32}$$

We define P_e and P_b as the usually-unknown overall efficiencies for electrons e and non-electrons b respectively, resulting from the trigger and selection efficiencies. It is convenient to rewrite Eq. (32) as

$$\rho(\mathbf{x}) = \frac{f_e(\mathbf{x})P_e}{f_b(\mathbf{x})P_b}. \tag{33}$$

If P_e and P_b were known, the cut $\rho > 1$ would give the optimal discrimination criterion. Since they are unknown, we work with the reduced likelihood ratio

$$\rho'(\mathbf{x}) = \frac{f_e(\mathbf{x})}{f_b(\mathbf{x})}. \tag{34}$$

Since our interest is to maximize the signal to background ratio rather than minimize the absolute number of misassignments, we empirically determine a suitable minimum value of ρ', depending on the analysis being performed. We refer to ρ' as the electron weight (EW). The measured quantities $\mathbf{x}$ included in the EW are:[24]

- **H1** pulse height corrected by θ.
- **H2** pulse height corrected by θ.
- **H2′** pulse height corrected by θ.
- **Č** Cherenkov pulse height, corrected by θ and mirror p.e. yield, independently for all 16 mirrors.
- s_θ, s_ϕ CCAL cluster second moment in wedge and ring directions, calculated using:

$$s_\theta = \frac{\sum_{r,w=1}^{3} E(r,w)*(w-w_0)^2}{\sum_{r,w=1}^{3} E(r,w)} \tag{35}$$

$$s_\phi = \frac{\sum_{r,w=1}^{3} E(r,w)*(r-r_0)^2}{\sum_{r,w=1}^{3} E(r,w)} \tag{36}$$

[24] We have omitted the fiber tracker dE/dx measurement to avoid correlations between tracking and particle identification. This measurement is one of 4 independent dE/dx measurements.

where index r runs over CCAL rings, w over wedges; $E(r,w)$ is the energy in block (r,w).

- F_{35} Ratio of the energy deposited in a 3×3 block matrix divided by that in a 5×5 block matrix, both surrounding the highest energy block in the cluster.
- F_{24} The same as F_{35} using matrices of sizes 2×2 and 4×4.
- $M_{\rm cl}$ Cluster mass as defined in Eq. (24).

For the CCAL variables s_θ, s_ϕ, F_{35}, F_{24} and $M_{\rm cl}$, all of the blocks surrounding that with the highest energy are used, whether or not the cluster is split.

To compute EW we take $f_e(\mathbf{x})$ and $f_b(\mathbf{x})$ as the (normalized) product of the measured distributions of each variable, for clean samples of electron and non-electron tracks. We assume that the EW variables $\mathbf{x}$ are uncorrelated, in order to factor $f_e(\mathbf{x})$ and $f_b(\mathbf{x})$ into individual pdfs $f_{\rm e}^i(x_i)$ and $f_b^i(x_i)$. Eq. (34) then becomes

$$\mathrm{EW}=\frac{\prod_i f_e^i(x_i)}{\prod_i f_b^i(x_i)}=\prod_i\frac{f_e^i(x_i)}{f_b^i(x_i)}=\prod_i W_i \tag{37}$$

so EW is the product of individual weights W_i.

The individual pdfs are determined from events selected by the trigger, Section 6. The tracks must consist of a CCAL cluster associated with at least two out of three hodoscope hits and a Cherenkov signal. For the electron pdfs, we take a clean sample of J/ψ and χ_2 events with consistent event topology and acceptable kinematic fit probability. For the background pdfs, we use events from runs taken well outside known resonance regions, namely at energies between 3590 and 3660 MeV (η_c' search). The pdfs and the weight distributions of the variables are plotted in Figs. 56–63.

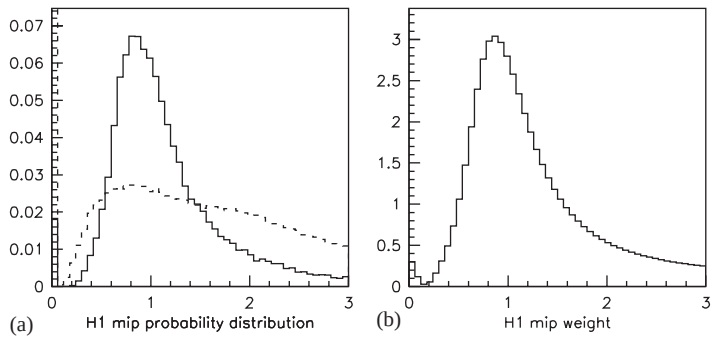

Fig. 56. (a) Probability density function for electrons (solid) and background tracks (dashed) and (b) weight distribution for H1 dE/dx.

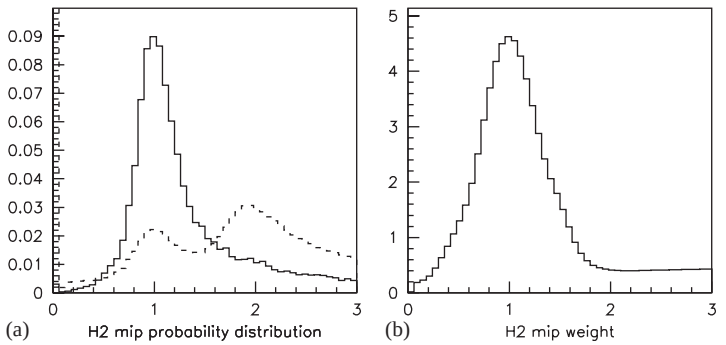

Fig. 57. (a) Probability density function for electrons (solid) and background tracks (dashed) and (b) weight distribution for H2 dE/dx.

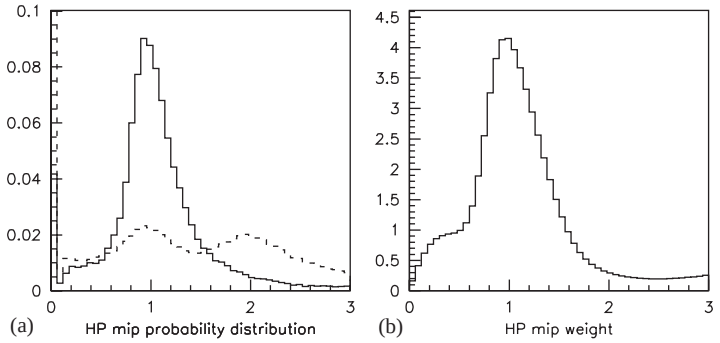

Fig. 58. (a) Probability density function for electrons (solid) and background tracks (dashed) and (b) weight distribution for H2′ dE/dx.

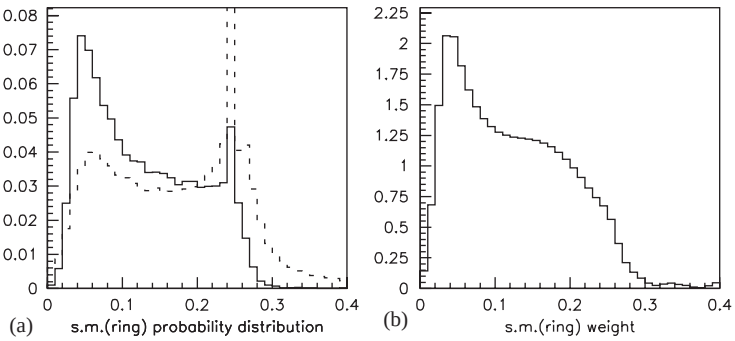

Fig. 59. (a) Probability density function for electrons (solid) and background tracks (dashed) and (b) weight distribution for the CCAL cluster second moment s_θ.

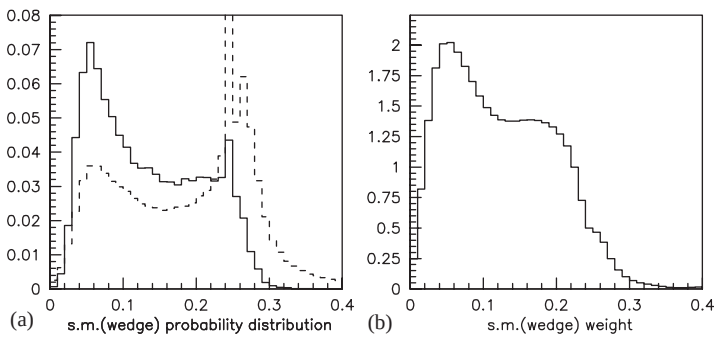

Fig. 60. (a) Probability density function for electrons (solid) and background tracks (dashed) and (b) weight distribution for the CCAL cluster second moment s_ϕ.

8.4.1. *Efficiency and background rejection*

All events of interest have either zero or two electrons in the final state; we work with the product of electron weights for both electrons. EW now refers to $EW_1\ EW_2$. We determine the EW cut empirically to yield the maximum signal to background ratio. We use an independent J/ψ sample to measure the efficiency of the electron-weight cut and a sample of events taken during the η_c' search to determine the background rejection power. Fig. 64 shows the distribution of EW for

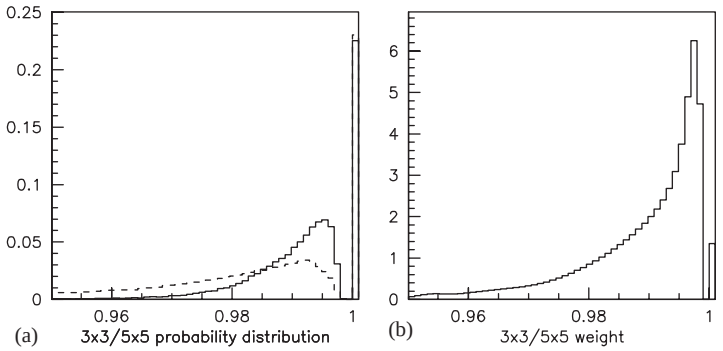

Fig. 61. (a) Probability density function for electrons (solid) and background tracks (dashed) and (b) weight distribution for the F_{35} variable.

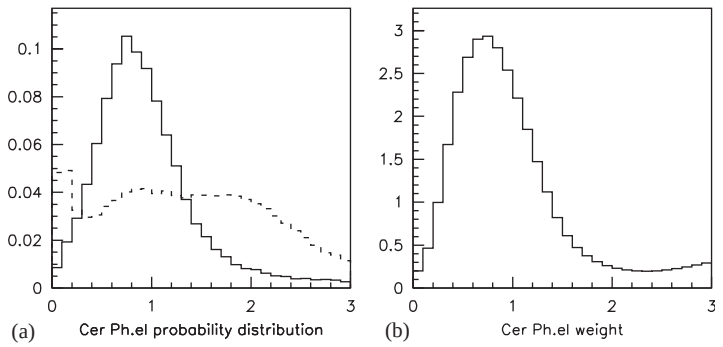

Fig. 62. (a) Probability density function for electrons (solid) and background tracks (dashed) and (b) weight distribution for the normalized Cherenkov p.e. yield.

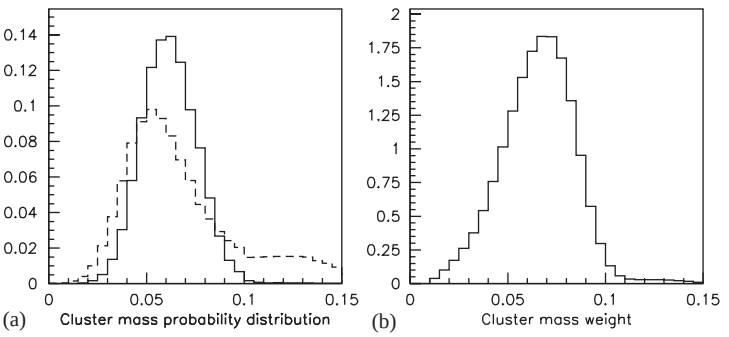

Fig. 63. (a) Probability density function for electrons (solid) and background tracks (dashed) and (b) weight distribution for the cluster mass M_{cl}.

electron and background tracks, and Fig. 65 shows the cumulative distributions. We have used EW cuts between 0.1 and 10.0, depending upon the purity required for the analysis

We demonstrate the effectiveness of this method in Fig. 66, where we plot the e^+e^- invariant mass for 10.9 pb^{-1} of integrated luminosity taken in the η_c' region ($\sqrt{s}$ between 3590 and 3660 MeV). A clear J/ψ inclusive peak is visible. We estimate the background cross-section for simulating $J/\psi \to e^+e^-$ inclusive events to be less than 6 pb.

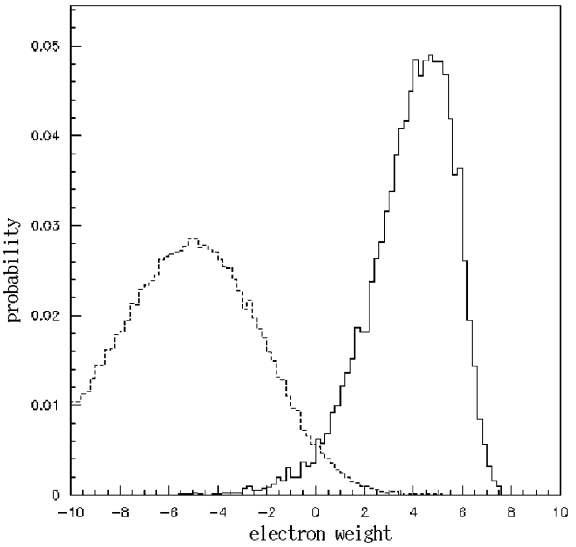

Fig. 64. Electron-weight distribution for electrons (solid) and background (dashed) tracks.

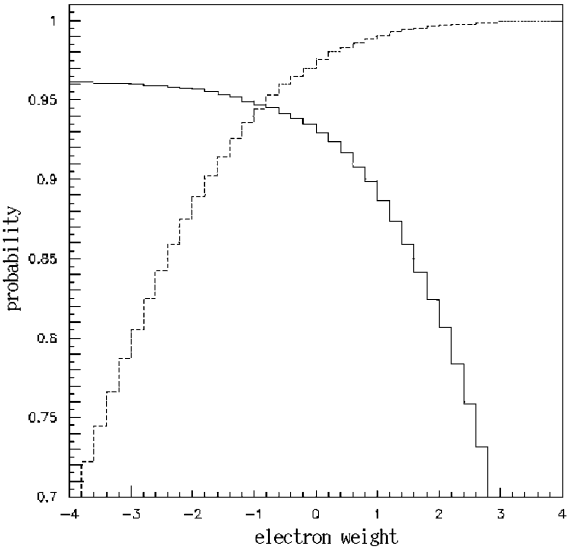

Fig. 65. Cumulative electron-weight distribution for electrons (solid) and background (dashed) tracks.

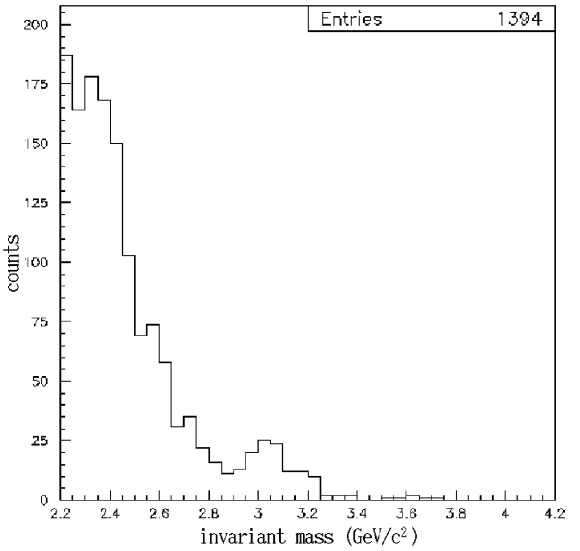

Fig. 66. Invariant mass distribution for inclusive e^+e^- events at a c.m. energy near 3640 MeV. The events are selected requiring EW > 10.

9. Simulations

Two simulations are used in the data analysis. We use GEANT 3.2 [37] for small simulated data sets and to compute acceptances and individual detector response properties. However when very large simulated data sets are required, mainly for all-neutral channels, we simulate events using a parametric description of the CCAL response. This simulation runs 10–20 times faster than GEANT and allows us to generate enough events to accurately study, for example, the background to $\gamma\gamma$ events. We describe the latter technique and discuss the comparison with data.

We randomly choose particle energies and directions to be consistent with the kinematics of the desired reaction. The event vertex is randomly chosen in the interaction region from a distribution based on the shapes of the beam and gas-jet target, and centered at the (x_0, y_0) measured for the data-point being simulated. The point (x', y') for each CCAL block struck by a particle is calculated. We simulate the CCAL response as follows and randomly choose the ADC value for each block.

The center of gravity of each cluster is calculated from (x', y') by inverting Eq. (22). The mean energy lost in CCAL cracks is calculated using Eq. (23) and subtracted. The distribution of the remaining energy about the cluster's center of gravity is modeled as the sum of two exponentials, shown in Fig. 67. This parameterization is chosen

empirically by comparing simulated events with $\pi^0\pi^0$ data taken at low instantaneous luminosity. The distribution is integrated to obtain the energy deposited in each block.

The energies lost in the cracks and deposited in CCAL blocks are smeared to simulate the energy resolution of the CCAL. A pedestal fluctuation is introduced for each block, based on the pedestal width measured for the stack of interest prior to taking data. The calibration constants for that stack are used to convert energies to ADC counts.

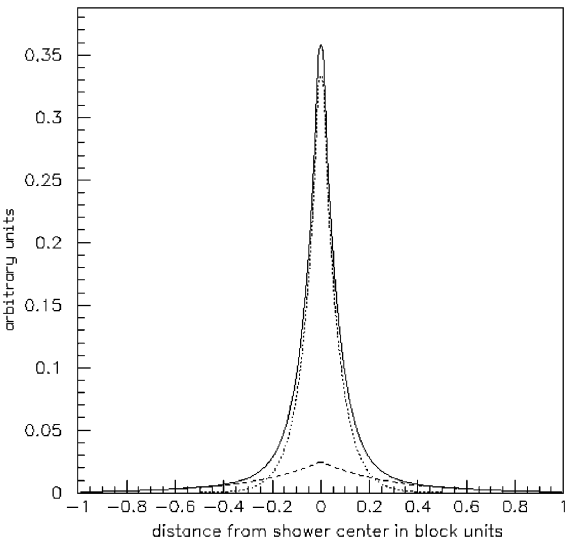

Fig. 67. The shower profile in the wedge direction used in the simulation. It is the sum of two exponentials, shown individually as dashed curves. The profile models the mean shower shape after the crack losses. The profile in the ring direction is slightly wider since less energy is lost in the cracks.

We simulate TDC information for the two blocks with the largest ADC values, i.e. those considered in determination of the cluster time. Counters with more than 50 ADC counts are assumed to have a TDC hit within the 20 ns window about T_0. For a counter with less than 50 ADC counts, we refer to its turn-on curve (see Fig. 50) and use a random number to determine whether TDC information exists. If so, we use an additional random number to determine whether the time is within the $T_0 \pm 10$ ns window using a table for all counters, created from $\pi^0\pi^0$ data, giving, for each ADC value, the fraction of TDC hits within the window. There are several counters for which there is a non-zero fraction of hits outside the window; the inefficiencies are found only for the smallest ADC values (values near A_0, see Eq. (29)).

Finally, to simulate the effect of overlapping events, we utilize the data collected with the random trigger. An event taken with the random trigger during the stack being simulated is superimposed onto the Monte Carlo event.

In Figs. 68 and 69, we compare the distributions of $\pi^0\pi^0$ analysis variable for the data and simulated events at the same data-point. The

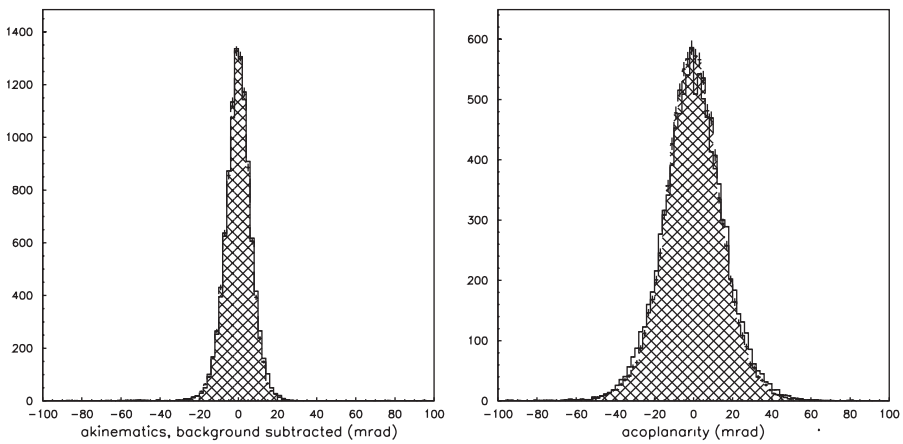

Fig. 68. Comparison of the akinematics and acoplanarity distributions for the $\pi^0\pi^0$ analysis showing data (unshaded) and simulated (shaded) events for a particular data point.

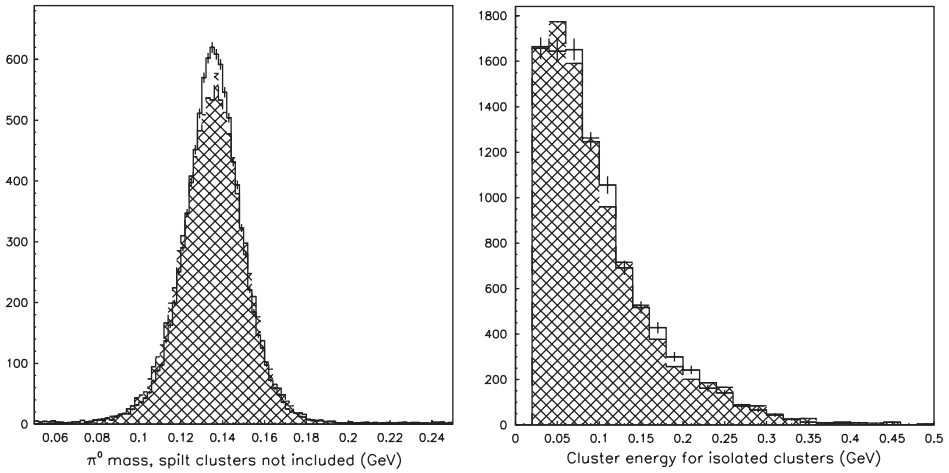

Fig. 69. Comparison of the π^0 mass and cluster energy distributions for the $\pi^0\pi^0$ analysis showing data (unshaded) and simulated (shaded) events for a particular data point.

distributions are normalized and the error bars are statistical.

Acknowledgements

A large number of people contributed to the design and construction of the detector and to the successful operation of the experiment.

We thank the Fermilab Beams Division and especially the Antiproton Accumulator people for their efforts to adapt the Accumulator to our experiment needs.

We thank the Fermilab Computing Division and in particular the Dart project led by R. Pordes for support with the data acquisition and online computing.

We thank members of the former Research Division for support in many areas.

D. Allspach, C. Kendziora and his group, and D.A. Miller have done a wonderful job on the jet target upgrade and maintenance.

T. Gasteyer and P. Wheelwright and the thermal systems group under R. Schmitt implemented the cryogenics system for the fiber detector. We are also in debt to A. Bross and S. Gruenendahl for their great support on the fiber tracker and VLPC design.

Members of the former Physics Section provided key support for the experiment electronics; in particular S. Hansen provided key DAQ electronics, and A. Prosapio and C. Rivetta provided the CCAL shaper boards.

The high quality work of the INFN engineers V. Carassiti, F. Daudo, G. Giraudo, and P. Musico has been very important.

We want also to acknowledge the valuable work done by the INFN and University technicians from Ferrara, Genova and Torino: G. Alfarone, G. Barisone, G. Bonora,[25] S. Chiozzi, G. Dughera, L. Milano, S. Minutoli, M. Negri, P. Poggi, E. Rosso, G. Scalise, and P. Trapani.

We thank our students and summer students: F. Albert, S. Hadley, M. Cardarelli, B. McDowell, J. Fenn, T. Schmidt, C. Teplin and J. Thywissen.

L. Bartoszek has done an invaluable work during the detector installations.

We thank M. Newcomer, M. Sancez and C. Millerin from CERN for their help on the straw chamber electronics.

Finally, we wish to acknowledge the contributions of our colleagues from experiment E760 which formed the essential basis for the work presented here.

[25] Sadly, Gabriele passed away on April 23rd, 1999.

This work has been supported by the Italian Istituto Nazionale di Fisica Nucleare (INFN) and by the US Department of Energy (DOE).

References

[1] T.A. Armstrong, et al., Fermilab Proposal P-835, September 2, 1992.
[2] T.A. Armstrong, et al., Phys. Rev. D 47 (1993) 772.
[3] R. Cester, P. Rapidis, Ann. Rev. Nucl. Part. Sci. 44 (1994) 329.
[4] C. Baglin, et al., Phys. Lett. 187 B (1987) 191.
[5] S. Chattopadhyway, in: Proceedings of Physics of High Energy Accelerators, AIP Conference Proceedings, Vol. 127, AIP, New York, 1985.
[6] C. Caso, et al., PDG 98, Eur. Phys. J. C 3 (1998) 1.
[7] D.A. Edwards, M.J. Syphers, An Introduction to the Physics of High Energy Accelerators, Wiley, New York, 1993.
[8] M. Macrí, CERN 84-15 (1984);
M. Macrí, in: T. Bressani (Ed.), Internal Gas Jet Targets for Nuclear and Particle Physics Experiments in Hadronic Physics at Intermediate Energies, Elsevier, Amsterdam, 1987.
[9] D. Allspach, et al., Nucl. Instr. and Meth. A 410 (1998) 195.
[10] O.F. Hagena, W. Obert, J. Chem. Phys. 59 (1972) 1793.
[11] J. Gspann, K. Korting, J. Chem. Phys. 59 (1973) 4726.
[12] LAMINA Dielectrics Ltd., England.
[13] F.M. Newcomer, et al., IEEE Trans. Nucl. Sci. NS-40 (1993) 630.
[14] D.C. Christian, et al., Nucl. Instr. and Meth. A 345 (1994) 62.
[15] S. Bagnasco, et al., Nucl. Instr. and Meth. A 409 (1998) 75.
[16] A. Buzzo, et al., Nucl. Instr. and Meth. A 391 (1997) 443.
[17] P. Musico, et al., Nucl. Instr. and Meth. A 420 (1999) 132.
[18] M. Ambrogiani, et al., IEEE Trans. Nucl. Sci. NS-44 (1997) 460.
[19] M. Ambrogiani, et al., Nucl. Instr. and Meth. A 419 (1998) 632.
[20] T. Zimmermann, et al., IEEE Trans. Nucl. Sci. NS-37 (1990) 339.
[21] W. Baldini, et al., IEEE Trans. Nucl. Sci. NS-48 (2001) 1122.
[22] C. Biino, et al., Nucl. Instr. and Meth. A 317 (1992) 135.
[23] S. Bagnasco, et al., Nucl. Instr. and Meth. A 424 (1999) 304.
[24] C. Biino, et al., Nucl. Instr. and Meth. A 235 (1985) 488.
[25] F. Garibaldi, Laboratorio di Fisica dell'Istituto Superiore di Sanita', Roma, Italy, private communication.
[26] L. Bartoszek, et al., Nucl. Instr. and Meth. A 301 (1991) 47.
[27] J.E. Fast, Ph.D. Thesis, University of California, Irvine, 1992.
[28] K.E. Gollwitzer, Ph.D. Thesis, University of California, Irvine, 1993.
[29] T.A. Armstrong, et al., Phys. Rev. D 52 (1995) 4839.
[30] M. Hasan, et al., Nucl. Instr. and Meth. A 295 (1990) 73.
[31] S. Trokenheim, et al., Nucl. Instr. and Meth. A 355 (1995) 308.
[32] T. Armstrong, et al., Phys. Lett. B 385 (1996) 479.
[33] W. Baldini, et al., Nucl. Instr. and Meth. A 449 (2000) 331.
[34] R. Ray, et al., Nucl. Instr. and Meth. A 307 (1991) 254.
[35] G. Oleynik, et al., IEEE Trans. Nucl. Sci. NS-41 (1994) 45.
[36] M. Pallavicini, et al., Nucl. Instr. and Meth. A 405 (1998) 133.
[37] GEANT-Detector Description and Simulation Tool; http://wwwinfo.cern.ch/asd/geant/.